EXPERIMENTAL EVALUATION OF FLUID-TO-FLUID SCALING MODELS FOR DETERIORATED HEAT TRANSFER AT SUPERCRITICAL PRESSURES

by
Benjamin Sears

A thesis submitted to the University of Ottawa
in partial fulfillment of the requirements for the degree of

MASTER OF APPLIED SCIENCE

in the Department of Mechanical Engineering
Faculty of Engineering
University of Ottawa

Abstract

Experimental evaluations of two fluid-to-fluid scaling methods for deteriorated heat transfer (DHT) in upward vertical flows in tubes at supercritical pressures were performed at the University of Ottawa Supercritical Heat Transfer Loop (SCUOL), using Refrigerant R134a as a medium at conditions that were determined by scaling those in previous carbon dioxide tests in the same loop. Two scaling methods were considered: the Ottawa method, which was based on local scaling, and the Pisa method, which was based on global scaling. Both methods were partially successful in scaling the occurrence or absence of DHT, but only when allowing for the thresholds of DHT onset conditions to span some ranges rather than being sharply defined. Both methods were inaccurate in predicting the exact location of DHT and the value of the heat transfer coefficient.

Acknowledgements

First and foremost, I would like to thank my supervisor, Professor Stavros Tavoularis, for his support and guidance over the course of my graduate studies. It has been an invaluable experience studying under such an experienced mentor.

I also would like to thank my thesis examiners, Professors R. St-Gelais and M. Yaras for their insightful feedback.

Additionally, the staff employed by uOttawa in the machine and electronics shops helped me overcome multiple hurdles when restarting the lab. Without their assistance and expertise, the lab would have never reached a functional state.

I thankfully acknowledge the funding for this research was provided by the Natural Sciences and Engineering Research Council of Canada (NSERC), which without would have made this undertaking impossible.

Lastly, I would like to thank all of my family and friends who have given me nothing but their constant support, time, and advice over the course of my studies. I could not have hoped to complete this work without you all.

Table of Contents

Nomenclature

Roman symbols

A	Area, m^2; cross-sectional
a, b	Coefficients
C_p	Specific heat at a constant pressure, J kg^{-1} K^{-1}
d	Test section inner diameter, mm
G	Mass flux, kg m^{-2} s^{-1}
g	Gravitational acceleration, m s^{-2}
H	Specific enthalpy, kJ kg^{-1}
h	Convective heat transfer coefficient, W m^{-2} K^{-1}
I	Current, A
k	Thermal conductivity, W m^{-1} K^{-1}
L	Length, m
$\dot{m}$	Mass flow rate, kg s^{-1}
N	Number of samples
Nu	Nusselt number = hd/k
P	Pressure, kpa, MPa

Pr Prandtl Number $= C_p\mu/k$

$\dot{Q}$ Heating power, W

q Heat flux, W M^{-2}

ΔQ Power imbalance, kW

Q_e Percent power imbalance error, %

R Electrical Resistance, Ω

r Radius, m

Re Reynolds number $= Gd/\mu$

T Temperature, °C, K

t Time, s

V Voltage, V

υ Velocity, m s^{-1}; specific volume, m^3 kg^{-1}

z_h Axial location, m

Greek letters

β Volumetric thermal expansion coefficient, K^{-1}

Δ Difference

μ Dynamic viscosity, kg m^{-1} s^{-1}; arithmetic mean

ν Kinematic viscosity, m^2 s^{-1}

ρ Density, kg m^{-3}

ρ_e Electrical resistivity, $\Omega \cdot$ m

σ Standard Deviation

Subscripts

av Average

b Bulk

C CO_2

c Critical

e Error

i Inner; index

in Inlet

lf Linear-least squares fit correction

max Maximum value

min Minimum value

o Outer

out Outlet

pc Pseudocritical

R R134a

ref Reference

W H_2O

w wall

1 Fluid one

2 Fluid two

RMS/rms Root mean square

Overbar

− Average between wall and bulk values

Abbreviations

CNL Canadian Nuclear Laboratories

CO_2 Carbon dioxide

DAS Data acquisition system

DHT Deteriorated heat transfer

EG Ethylene Glycol

EHT Enhanced heat transfer

Gen-IV Generation IV

GIF Generation IV International Forum

GWP Global warming potential

H_2O Chemical formula of water

HE Heat exchanger

HTC Heat transfer coefficient

HTD Heat transfer deterioration

I.D./ID Inter diameter

NHT Normal heat transfer

NIST Thermophysical properties software of different fluids (Lemmon *et al.*, 2002)

ODP Ozone-depleting potential

OPPSEC Ozone Protection Programs Section Environment Canada

PR Pressure ratio

PT Pressure transducer

R134a HFC Refrigerant R134a (Freon)

RTD Resistance temperature detector

SC Supercritical

SCUOL Supercritical University of Ottawa Loop

SCWR Supercritical water reactor

SMR Small modular reactor

STD Standard deviation

TC Thermocouple

TC-LUT Trans-critical look-up tables

TS Test section

Vt Vent

Chapter 1

Introduction

1.1 Motivation for this research

The Canadian nuclear power industry is currently in the middle of a paradigm shift. There has been a renewed interest in established CANDU nuclear reactor technology, as well as development and assessment of small modular reactor (SMR) designs, some of which are adopting entirely new technologies. Traditionally, the industry has focused on building large power generating stations, composed of multiple reactors that are individually capable of producing hundreds of megawatts of electric power. This approach has centralised the electricity production, making it available through national scale power grids. The drawback of centralised production is that, if a plant is cut off from the grid due to an accident, maintenance or other reason, there may not be sufficient alternative sources of electricity production to prevent regional blackouts. The use of SMRs alleviates this limitation of traditional nuclear power generation. SMRs are relatively low power nuclear reactors, which are modular by design, so that they can be used individually or together in banks for high power output requirements. This concept allows electricity production to be scalable and decentralised from large power generating sites. Localised electricity production increases the reliability of the power grid: if a plant fails, an outage does not impact a large proportion of the grid power and the lost power could potentially be rerouted from other parts of the grid that produce excess, thus preventing blackouts altogether.

Smaller sites also provide an opportunity for remote locations to have access to clean energy production, as opposed to using fossil-fuel based electric generators. Generation IV nuclear technology is at the forefront of the design of SMRs in the nuclear power industry. These are novel reactor concepts, which are all considered to be advancements of current technology in the industry, each concept providing a unique set of benefits. Among these concepts, the one of interest in the present work is the Supercritical Water-cooled Reactor (SCWR) and the recently introduced SCW SMR concept (Jevremovic & Rehman, 2021; ECC-Smart & ENEN, 2020). The following list highlights some of the benefits of SCWR by comparison to current nuclear reactor technologies.

- More economic operation due to higher coolant operating temperature, which leads to increased thermodynamic cycle efficiency.
- Simpler plant design and operating procedures.
- Improved safety.

Heat transfer measurements in channels cooled by water at near-critical pressures, collected in a specialized facility at the University of Munich, Germany, have recently been reported by Oettig *et al.* (2024). Additionally, there is a pursuit of supercritical SMR designs by South Korea and Japan in the form of a supercritical CO_2 SMR (Son & Lee, 2024; Uchimura & Yamaji, 2020). Beside their use in supercritical nuclear reactors, supercritical fluids are used in water-cooled, coal-fired power plants, for production of fuel-grade hydrogen by fluid decomposition, for extraction of active ingredients such as caffeine, flavours and fragrances, as solvents in chemical reactions, for processing and preserving food products, in pharmaceutical industries to create nano- and micro-particles, and for hazardous waste treatment. In view of the complex behaviour and the numerous applications of supercritical fluids, the understanding and prediction of their thermophysical behaviour and heat transfer characteristics is of great scientific and practical importance.

As mentioned previously, collecting heat transfer data for supercritical (SC) water is a challenging task, due to the extreme pressure and temperature required for

water to exist in the SC state. Water has a critical pressure of 22 MPa and a critical temperature of 374°C. Due to the technical challenges and high cost associated with making a SC water facility, fluid-to-fluid similarity theories have been developed to allow the prediction of SC water behaviour by scaling data from other fluids. Among the many fluids that have been considered, carbon dioxide and Refrigerant R134a (freon) have been found to be suitable surrogates for water, because they have critical pressures and temperatures that are much lower than those of water as well as thermophysical properties with trends near the corresponding critical points, which are comparable to those of water. Scaling data from one fluid to another requires the development of scaling correlations. SC heat transfer may be classified as normal (NHT), enhanced (EHT) or deteriorated (DHT). DHT is a breakdown in normal heat transfer that, at least in the case of upwards vertical pipe flow, is characterised by localised wall temperature spikes and, if allowed to persist, may lead to overheating and eventually melting of the pipe wall. Avoiding DHT is of main concern in SCWR design. Although this topic has been studied for a long time, development of DHT correlations and prediction of DHT remain challenging issues. A main objective of fluid-to-fluid scaling is to allow the prediction of the heat transfer coefficient in one fluid by scaling its value under equivalent conditions in another. Current methods allow this within tolerable uncertainty for NHT, but the reliable prediction of DHT occurrence and the heat transfer coefficient under DHT conditions in one fluid by scaling data in another remains an issue of active investigation and will be discussed in this thesis.

Among previously developed fluid-to-fluid scaling procedures, our interest concentrates on one that will hereafter be referred to as the *Ottawa method* (Zahlan *et al.*, 2014) and another, to be referred to as the *Pisa method* (Pucciarelli & Ambrosini, 2020). These procedures engage a mix of arguments that are based on theoretical, experimental and computational bases. They have been tested in different working fluids, including water, carbon dioxide and refrigerant R134a. The works of Zahlan *et al.* (2014), Mouslim (2019), Kline (2017), Watts & Chou (1982), and Pucciarelli & Ambrosini (2020) are most relevant to the current discussion and valuable sources of supercritical fluid data and fluid-to-fluid scaling methods. To evaluate these two

methods, we will assess the degree by which they satisfy the following two requirements.

- First, a weak requirement: is the scaling method successful in predicting that, when one fluid exhibits NHT in the entirety of the channel, so will the other, and furthermore that, when one fluid exhibits DHT in some part of the channel, so will the other? In other words, a method will not satisfy this weak requirement, if it cannot separate cases with NHT from those with DHT along the channel, irrespective of whether its prediction of heat transfer coefficient is accurate or not.

- Second, a strong requirement: is the scaling method able to predict the local value of the heat transfer coefficient with some accuracy under DHT conditions?

The success of any test of a scaling method is intimately connected to the adopted DHT detection criterion. Among the several suggested criteria for DHT detection, we followed the approach adopted by Kline *et al.* (2018), namely that DHT occurs in sections of the channel, where there is a peak (or bump) in the wall temperature axial profile. It seems then plausible that heat transfer reverts to the normal state downstream of such peak.

Kline (2017) investigated DHT in SC CO_2, assembling a large, high quality data set for both NHT and DHT conditions. This is invaluable in the present work, as readily available DHT data is not easily available in the literature. The scaling laws from Zahlan *et al.* (2014) (Ottawa method) were used by Mouslim (2019) with moderate success for scaling heat transfer in CO_2 to heat transfer in R134a. Mouslim (2019) examined a database that includes 21 NHT CO_2 profiles (34 scaled points) for all of which NHT R134a profiles were observed; this means that no NHT profile in CO_2 produced a scaled DHT profile in R134a. The database also includes 6 DHT CO_2 profiles (8 scaled points) for which the scaled points were downstream of the end of the bump, thus, presumably, in a region of the R134a channel where heat transfer resumed a NHT state; thus, we may add these points to the previous category, which includes NHT cases in both fluids. The database further includes 2 DHT CO_2 profiles (7 scaled points) for which the scaled points were on the bump; in all these cases, the

R134a profile had a distinct peak upstream of the scaled point, which clearly indicates the occurrence of DHT. All cases presented so far conform with the pattern that the Ottawa method produces local NHT in R134a, when the chosen point in CO_2 was in NHT, and local DHT in R134a, when the chosen point in CO_2 was in DHT. However, the database also includes a single DHT CO_2 profile (5 scaled points, Figure 5 in the article by Mouslim & Tavoularis (2019)), for which the R134a profile was entirely in NHT, irrespective of whether the chosen point in CO_2 was in the peak region or downstream of it. In view of all other results, this case appears to be peculiar and will be revisited in the present study. Even if we temporarily disregard this case, the available results indicate that, for the Ottawa method to predict DHT in R134a by scaling a flow with DHT in CO_2, one must scale a point in the DHT region and not downstream of it.

In their recent work, Pucciarelli & Ambrosini (2020) (Pisa method) have developed a fluid-to-fluid scaling method using CFD as the basis for its validation. The Pisa method follows an approach that is different from that of the Ottawa method: scaling in the former is enforced for the inlet conditions and is expected to apply to the entire channel, rather than at an isolated point, as for the latter. If adequately validated, the Pisa method has the potential of detecting DHT in a fluid, based on the occurrence of DHT at equivalent inlet conditions in another. The Pisa method has so far been tested positively by comparing measurements in CO_2 and computational results for R134a using a specific turbulence model but has not yet received a direct experimental validation.

1.2 Objectives and plan of the work

The objective of this research is to collect additional heat transfer measurements in a vertical upward flow of SC R134a in a circular tube and to use these and previously acquired data to further evaluate the Ottawa and Pisa fluid-to-fluid scaling methods, particularly under deteriorated heat transfer conditions.

The plan for carrying out this work is as follows:

- To recommission the Supercritical uOttawa Loop (SCUOL) for tests in SC R134a.

- To put together a test matrix of experimental conditions that are suitable for the present objectives.
- To collect experimental results in SC R134a that permit the testing of the Ottawa and Pisa scaling methods in the DHT regime.
- To test these scaling methods, identifying their successes and shortcomings, and to suggest possible improvements and areas for future work.

1.3 Thesis organisation

This thesis is composed of six chapters. Chapter 1 outlines the motivation for the research, introduces the fluid-to-fluid scaling methods for supercritical heat transfer and states the objectives and organisation of this thesis. Chapter 2 provides some background information on supercritical heat transfer and heat transfer deterioration, compares the thermophysical properties of water, CO_2 and R134a, and outlines the fluid-to-fluid scaling methods to be tested. Chapter 3 describes the experimental apparatus, instrumentation used and measurement procedures. Chapter 4 describes the selection of test conditions and the scaling of properties in the different test cases. Chapter 5 describes the results obtained from the experiment, and compares them with the predictions of the scaling methods. Chapter 6 summarises the main conclusions of the thesis and recommendations for future work.

Chapter 2

Background

2.1 Supercritical fluids

A supercritical fluid is a fluid that has a pressure that is larger than its critical value. The critical point of a fluid is the point on a temperature-pressure phase diagram, where the line separating the liquid and gas phases ends. Past the pressure at the end of the line, the liquid and gas phases become indistinguishable from each other. At SC pressures, the fluid diffuses through porous solids like a gas, but also acts as a solvent like a liquid. The phase diagram for water is shown in Figure 2.1, taken from Pioro *et al.* (2011). For every SC pressure, their exists a temperature, called the pseudo-critical temperature, at which the specific heat of the fluid is maximum. The locus of pseudocritical points is an extension of the saturation line, shown in Figure 2.1. The physical properties of SC fluids are very sensitive to temperature and pressure near the pseudo-critical temperature. Specifically, small changes in either temperature or pressure result in substantial changes of fluid properties, as seen in Figure 2.2. This is a challenge for engineers considering to use supercritical fluids in nuclear power systems as a coolant, because coolant thermophysical behaviour must be predictable and controllable accurately.

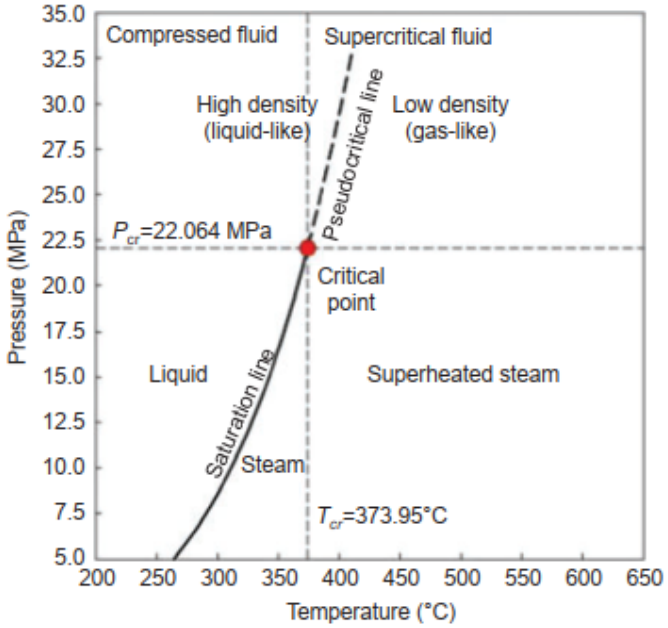

Figure 2.1: Phase diagram of water (Pioro *et al.*, 2011)

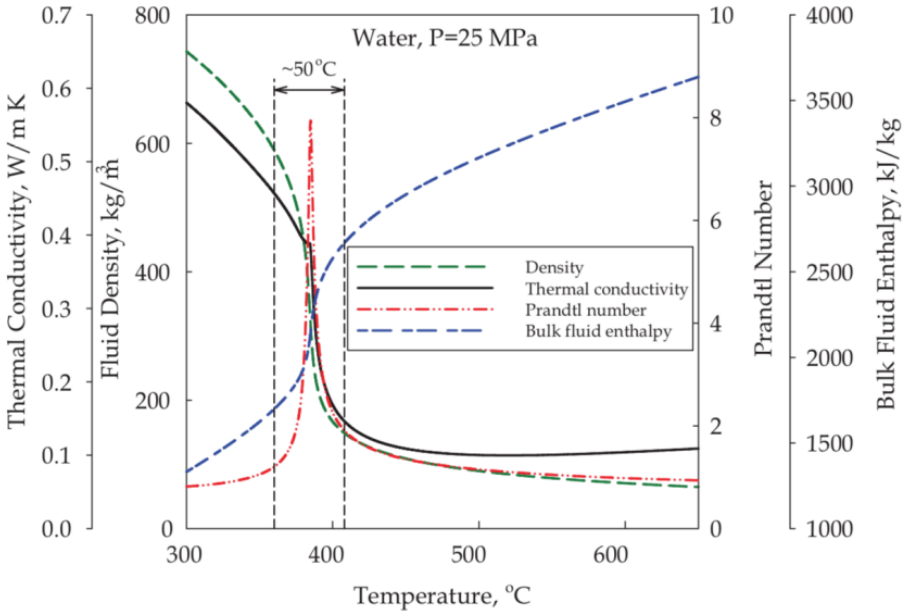

Figure 2.2: Temperature dependence of thermophysical properties of water at $P = 25$ MPa (Pioro *et al.*, 2011)

2.2 Comparison of the thermophysical properties of CO_2, R134a, and water

Current data found in the REFPROP materials data base compiled by Lemmon *et al.* (2002) show that both CO_2 and R134a have thermophysical properties that behave similarly to those of water near the corresponding pseudo-critical temperatures. A comparative analysis of the database and trends in thermophysical properties for CO_2 and R134a has been presented in many other works, including Pioro & Duffey (2007), Mouslim (2019), and Kassem *et al.* (2021). Although trends were close in some cases, depending on the scaling parameter used, they never exactly collapsed onto each other. This means that any potential fluid-to-fluid scaling method will at best be approximate. Relevant properties used in fluid-to-fluid scaling approaches are density, viscosity, thermal conductivity, enthalpy, volume expansivity, specific heat, and Prandtl number. Graphs taken from Pioro & Duffey (2007) for these properties of CO_2 and R134a near the critical temperature are shown in Figures 2.3 to 2.16.

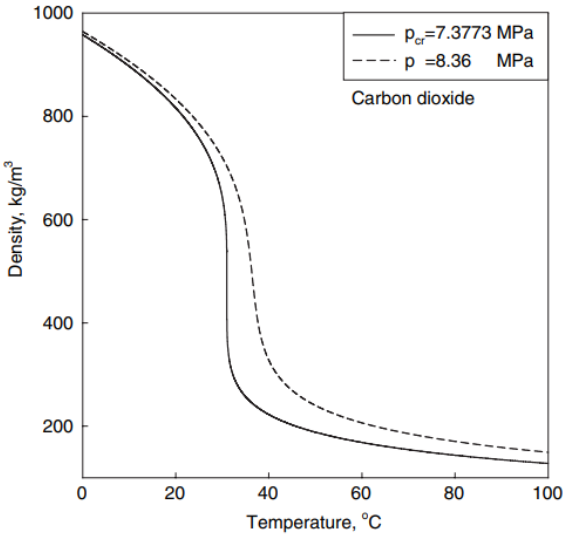

Figure 2.3: Variation of density for CO_2 vs temperature (Pioro & Duffey, 2007)

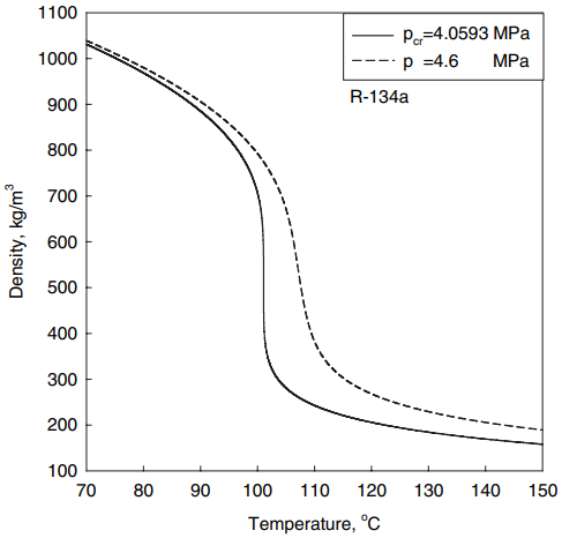

Figure 2.4: Variation of density for R134a vs temperature (Pioro & Duffey, 2007)

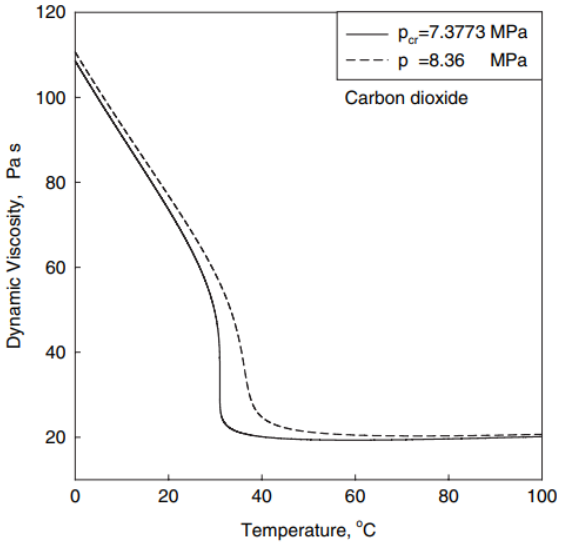

Figure 2.5: Variation of dynamic viscosity for CO_2 vs temperature (Pioro & Duffey, 2007)

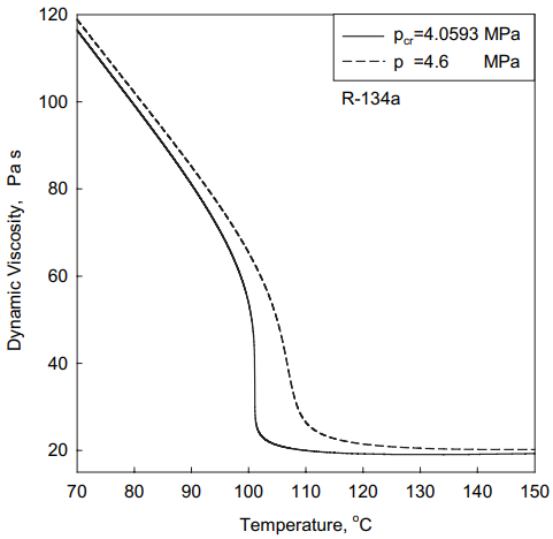

Figure 2.6: Variation of dynamic viscosity for R134a vs temperature (Pioro & Duffey, 2007)

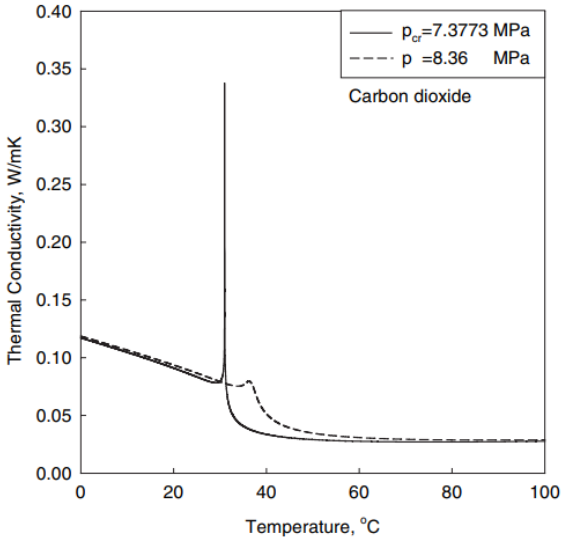

Figure 2.7: Variation of thermal conductivity for CO_2 vs temperature (Pioro & Duffey, 2007)

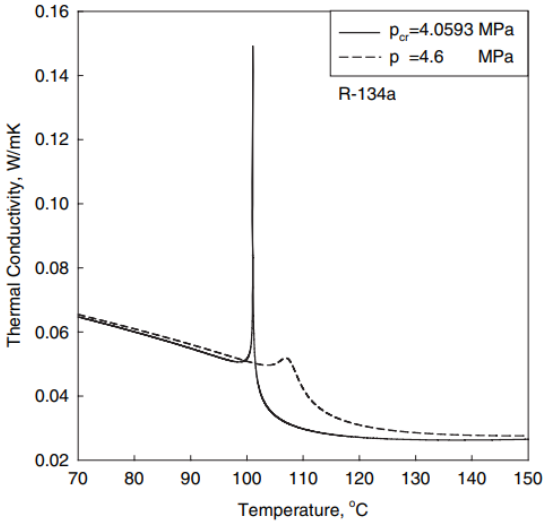

Figure 2.8: Variation of thermal conductivity for R134a vs temperature (Pioro & Duffey, 2007)

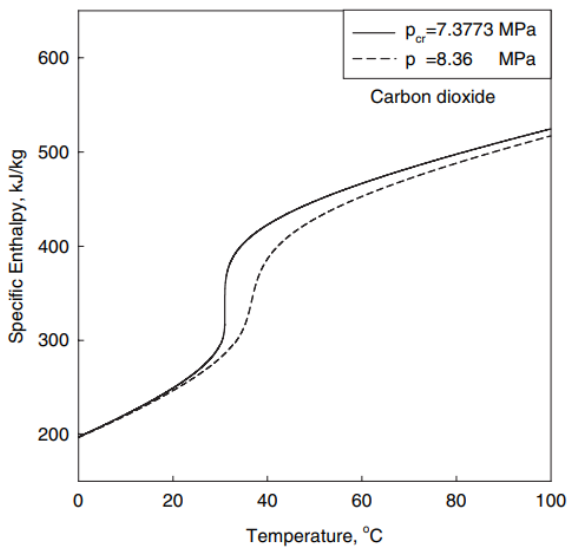

Figure 2.9: Variation of specific enthalpy for CO_2 vs temperature (Pioro & Duffey, 2007)

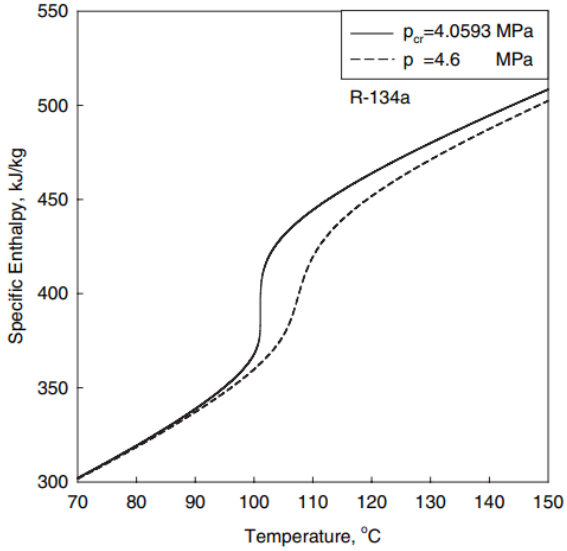

Figure 2.10: Variation of specific enthalpy for R134a vs temperature (Pioro & Duffey, 2007)

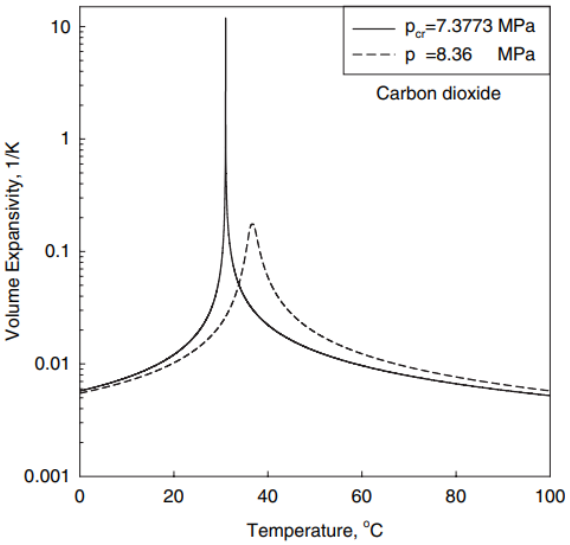

Figure 2.11: Variation of volume expansivity for CO_2 vs temperature (Pioro & Duffey, 2007)

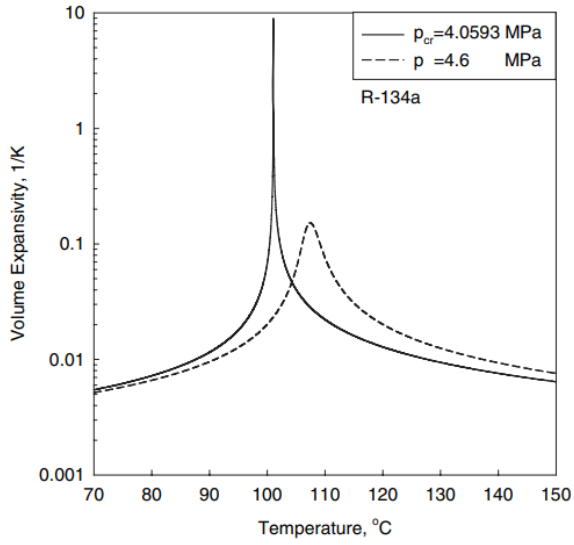

Figure 2.12: Variation of volume expansivity for R134a vs temperature (Pioro & Duffey, 2007)

2.3 Heat transfer in supercritical fluids

Heat transfer at supercritical pressures in vertical pipes has been observed to occur in three modes, which are referred to as normal heat transfer (NHT), deteriorated

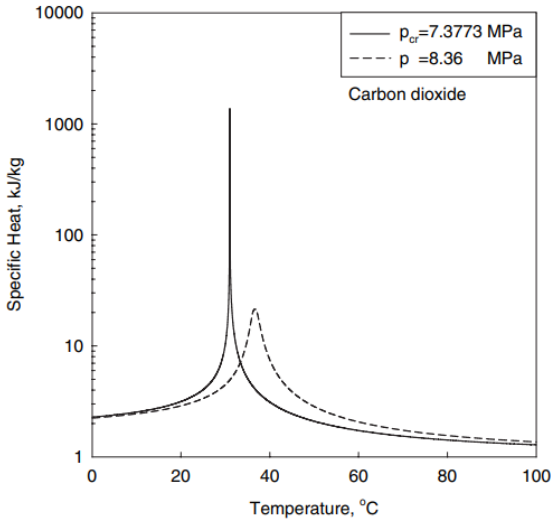

Figure 2.13: Variation of specific heat for CO_2 vs temperature (Pioro & Duffey, 2007)

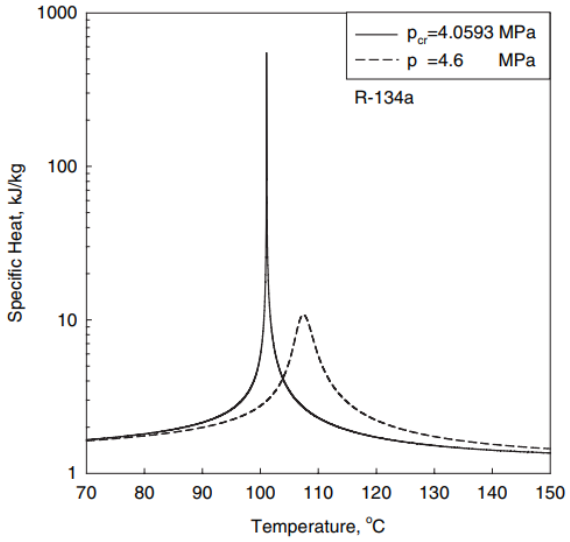

Figure 2.14: Variation of specific heat for R134a vs temperature (Pioro & Duffey, 2007)

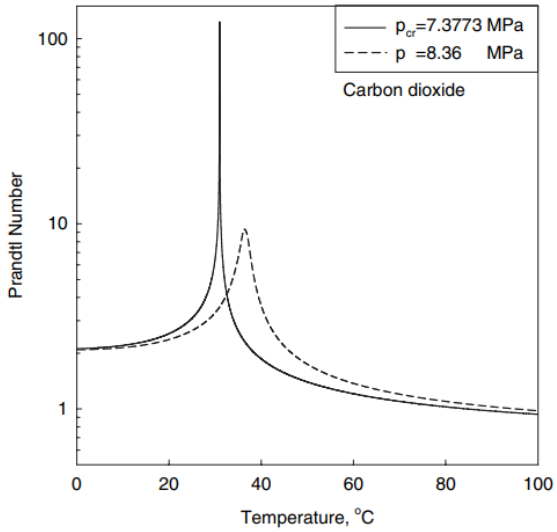

Figure 2.15: Variation of Prandtl number for CO_2 vs temperature (Pioro & Duffey, 2007)

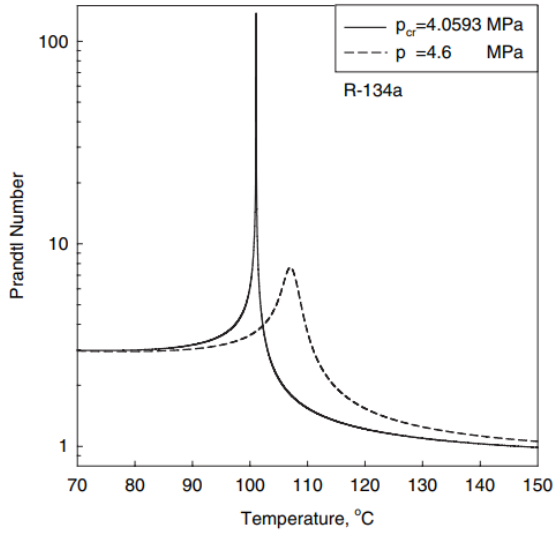

Figure 2.16: Variation of Prandtl number for R134a vs temperature (Pioro & Duffey, 2007)

heat transfer (DHT) and enhanced heat transfer (EHT). NHT follows trends similar to those of heat transfer in subcritical fluids. DHT, however, is a breakdown in heat transfer, causing an increase in pipe wall temperature and poor distribution of heat transfer throughout the pipe flow. Jackson & Hall (1978), suggested that, in many

cases of DHT, its onset is in part caused by a change in the structure of turbulence in the near wall region. This change in turbulence is attributed to a change in buoyancy of the fluid. In the case of an externally heated vertical tube, the density of the fluid closest to the wall is lower than that of the fluid in the core. This change in density causes a greater buoyancy force and a corresponding decrease in local mean shear, thus impeding transverse turbulent transport. As transverse turbulent transport decreases, the radial heat transfer rate decreases as well, and sudden increases in wall temperature are observed. In order to quantify the onset of DHT, Jackson & Hall (1978) suggested using a buoyancy parameter. The prediction of DHT is beyond the scope of the present work. Interested readers are directed to the work of Kline & Tavoularis (2021), which pursues the concept of using a buoyancy parameter to identify DHT using supercritical CO_2. Lastly, EHT is characterised by a drop in wall temperature. According to Kline (2017), EHT commonly occurs downstream of a wall temperature spike characteristic of DHT. The wall temperature profiles shown in Figure 2.17 (Kline, 2017) highlight each of these heat transfer modes.

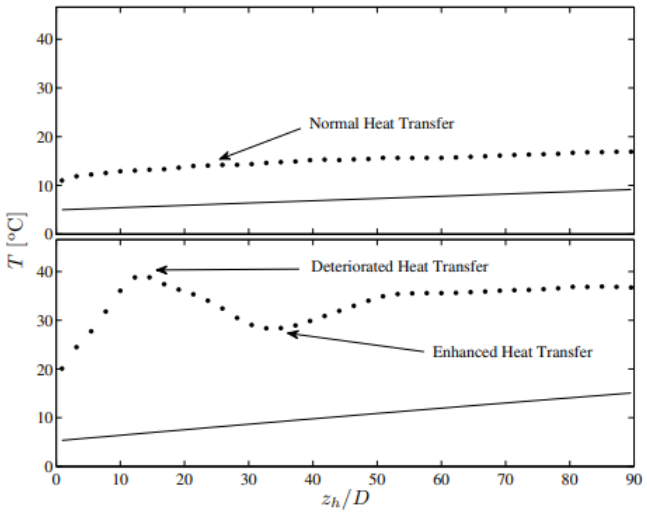

Figure 2.17: Wall temperature profiles along a heated tube, highlighting features of NHT, DHT, and EHT in CO_2; the solid line is bulk fluid temperature (Kline, 2017)

2.4 Fluid-to-fluid scaling methods

This section reviews various fluid-to-fluid scaling methods used in previous literature. A similar review was presented by Mouslim (2019). Our interest focuses on two methods, which were previously referred to as the Ottawa method and the Pisa method.

2.4.1 The Ottawa method

The Ottawa method, which has been described by Zahlan *et al.* (2014), is a modified version of the method described by Cheng *et al.* (2011), which will be outlined first. Cheng *et al.* (2011) presented a set of fluid-to-fluid scaling laws based on local bulk conditions, derived from the continuity, momentum, energy and surface heat transfer equations. The dimensionless temperature is scaled by the difference between pseudocritical and critical temperatures, which was found to perform better than scaling with either the pseudocritical or the critical temperature. This scale, however, produces a singularity at the critical pressure, which causes significant errors. Cheng *et al*'s method also scales the mass flux using the Dittus-Boelter correlation, which was developed using data at low subcritical pressures and is inaccurate at supercritical pressures, particularly for temperatures near the pseudocritical value. To avoid any dependence of the heat transfer coefficient upon the heated length, the entrance effect is neglected, potentially leading to further inaccuracy. The set of scaling equations proposed by Cheng *et al.* (2011) are shown below:

$$d_1 = d_2, \tag{2.1}$$

$$\left(\frac{P}{P_c}\right)_1 = \left(\frac{P}{P_c}\right)_2, \tag{2.2}$$

$$\left(\frac{T_b - T_{pc}}{T_{pc} - T_c}\right)_1 = \left(\frac{T_b - T_{pc}}{T_{pc} - T_c}\right)_2, \tag{2.3}$$

$$\left(\frac{GdPr_b^{\frac{5}{12}}}{\mu_b}\right)_1 = \left(\frac{GdPr_b^{\frac{5}{12}}}{\mu_b}\right)_2, \tag{2.4}$$

$$\left(\frac{qd}{k_b(T_{pc} - T_c)}\right)_1 = \left(\frac{qd}{k_b(T_{pc} - T_c)}\right)_2, \text{ and} \tag{2.5}$$

$$(Nu_b)_1 = (Nu_b)_2 \text{ or } \left(\frac{hd}{k_b}\right)_1 = \left(\frac{hd}{k_b}\right)_2, \tag{2.6}$$

where d is the internal pipe diameter, P is pressure, T is temperature, G is mass flux, Pr is the Prandtl number, μ is dynamic viscosity, q is the heat flux, k is thermal conductivity of the wall, Nu is the Nusselt number, and h is the heat transfer coefficient. Subscripts b, c, and pc refer to, respectively, bulk conditions, critical conditions, and pseudocritical conditions.

The Ottawa method (Zahlan *et al.*, 2014) has two main differences from the previous one:

- T_{pc} is used instead of the difference $T_{pc} - T_c$ to scale the temperature, thus avoiding a singularity near the critical pressure.
- The heat transfer correlation, which was used to scale the mass flux, was modified to apply to high subcritical and supercritical pressures.

Thus, the scaling equations for the Ottawa method are as follows:

$$d_1 = d_2, \tag{2.7}$$

$$\left(\frac{P}{P_c}\right)_1 = \left(\frac{P}{P_c}\right)_2, \tag{2.8}$$

$$\left(\frac{T_b}{T_{pc}}\right)_1 = \left(\frac{T_b}{T_{pc}}\right)_2, \tag{2.9}$$

$$\left(\frac{GdPr_b^{0.66}}{\mu_b}\right)_1 = \left(\frac{GdPr_b^{0.66}}{\mu_b}\right)_2, \tag{2.10}$$

$$\left(\frac{qd}{k_b T_{pc}}\right)_1 = \left(\frac{qd}{k_b T_{pc}}\right)_2, \text{ and} \tag{2.11}$$

$$(Nu_b)_1 = (Nu_b)_2 \text{ or } \left(\frac{hd}{k_b}\right)_1 = \left(\frac{hd}{k_b}\right)_2. \tag{2.12}$$

A drawback of the Ottawa method is that it is based upon local conditions, which implies that heat transfer at every point along a flow channel needs to be scaled individually. It would be obviously preferable to develop a scaling method which applies to the entire channel.

2.4.2 The Azih and Yaras scaling method

The method proposed by Azih & Yaras (2017) scaled fluid conditions at the inlet of the channel instead of locally at different points along the channel. This provides the advantage of reducing calculations by scaling only one point, the inlet, and allowing for similarity along the entire flow channel. The set of equations used in this method are as follows:

$$\left(\frac{P_{in}}{P_c}\right)_1 = \left(\frac{P_{in}}{P_c}\right)_2, \tag{2.13}$$

$$\left(\frac{(H_{in} - H_{pc})\beta_{pc}}{C_{p,pc}}\right)_1 = \left(\frac{(H_{in} - H_{pc})\beta_{pc}}{C_{p,pc}}\right)_2, \tag{2.14}$$

$$\left(\frac{Gd}{\mu_{in}}\right)_1 = \left(\frac{Gd}{\mu_{in}}\right)_2, \text{ and} \tag{2.15}$$

$$\left(\frac{q\beta_{pc}}{GC_{p,pc}}\right)_1 = \left(\frac{q\beta_{pc}}{GC_{p,pc}}\right)_2 . \tag{2.16}$$

The validity of scaling is verified by ensuring the equality of Richardson numbers, which is expressed as

$$\left(\frac{g\beta_{in}q(\rho_{in}d)^2}{k_{in}G^2}\right)_1 = \left(\frac{g\beta_{in}q(\rho_{in}d)^2}{k_{in}G^2}\right)_2 , \tag{2.17}$$

where β is the volumetric expansion coefficient and C_p is the specific heat.

2.4.3 The Pisa scaling method

The Pisa scaling method (Pucciarelli & Ambrosini, 2020), like the method of Azih & Yaras (2017), scales the inlet conditions of the flow channel. It imposes the following scaling conditions:

$$(N_{TPC})_1 = (N_{TPC})_2, \tag{2.18}$$

$$(N_{SPC})_1 = (N_{SPC})_2, \tag{2.19}$$

$$Fr_1 = Fr_2, \tag{2.20}$$

$$(Re_{in})_1 = (Re_{in})_2, \tag{2.21}$$

$$(\overline{Pr}^{-1/3}L/d)_1 \approx (\overline{Pr}^{-1/3}L/d)_2, \tag{2.22}$$

where

$$N_{TPC} = (\dot{Q}/\dot{m})\beta_{pc}/C_{p,pc}, \tag{2.23}$$

$$N_{SPC} = -H^*_{in} = -(H_{in} - H_{pc})\beta_{pc}/C_{p,pc}, \tag{2.24}$$

$$Fr = \upsilon^2/gd, \tag{2.25}$$

$$Re = (\rho\upsilon d)/\mu, \tag{2.26}$$

$$\overline{Pr} = \frac{\overline{C}_p\mu}{k} \ . \tag{2.27}$$

In these expressions, $\dot{Q}$ is the channel power, $\dot{m}$ is the mass flow rate, υ is the fluid velocity, H is the enthalpy, g is the gravitational acceleration, L is the test section length and superscript $*$ denotes dimensionless parameters. Quantities with an overline are averaged between bulk and wall values.

The authors of this theory define similar conditions as "two different fluid conditions under which the spatial distributions of the dimensionless enthalpy in the channel are the same or nearly the same." To achieve such similarity, they introduced two dimensionless parameters, the trans-pseudocritical number N_{TPC} and the pseudo-subcooling number N_{SPC}. Equality between the corresponding values of these two parameters ensures similar bulk specific enthalpy profiles along the channel and ensures heat transfer similarity for the two fluids.

The Pisa scaling method has so far been validated using results of numerical simulations with the commercial finite-volume CFD code STAR-CCM+ and the RANS (Reynolds-Averaged Navier-Stokes) turbulence modelling approach (Ambrosini, 2011; Pucciarelli & Ambrosini, 2016, 2020; Kassem *et al.*, 2021). In CFD simulations, it is easy to change the diameter and the length of a heated tube model, but, in an experimental setup, one would be restricted to using a single test section or, at most, a small number of test sections. Consequently, while performing experimental tests of this method with different fluids, one cannot keep both the Froude numbers and the Reynolds numbers equal at the inlet. In the present experiments, we collected measurements in CO_2 and R134a flowing through the same test section ($d_1 = d_2$). It turned out, however, that the inlet Froude numbers were close to each other (within 10%) for all test cases run, despite the equality of the diameters. This means that the inertial and buoyancy effects for the two fluids will not be identical, but will differ by some amount. The consequences of this difference will be considered when analysing the results. An additional constraint for the present experiments is that the ratio

L/d was fixed to a constant value. This may not be important for relatively long tubes, because they may contain the region where the phenomena of interest occur (Pucciarelli & Ambrosini, 2020).

A common point between the Ottawa and Pisa methods is that they both use pseudocritical conditions to scale various parameters. On the other hand, the two methods have the following main differences:

- The Ottawa method uses point by point scaling, whereas the Pisa method uses inlet conditions to scale the entire channel.
- The Pisa method formulation forces the equality of the ranges of dimensionless enthalpy in the two fluids.
- The Pisa method enforces equality of the inlet Reynolds numbers, whereas the Ottawa method equates the normalised mass flow rates,

Chapter 3

Experimental facility, instrumentation, and measurement procedures

3.1 Experimental facility

The experimental facility used in the present work is the Supercritical University of Ottawa Loop (SCUOL), the details of which can be found in the MASc theses by Jiang (2015), Kline (2017) and Mouslim (2019). The configuration used for this work, shown in figure 3.1, is specific for using R134a as the working fluid (Mouslim, 2019), whereas the configurations described by Jiang and Kline were using CO_2 as the working fluid. The apparatus used in all previous experiments in SCUOL was, however, relocated to a new building. Following relocation, some changes to the system were made. Due to a faulty connection of the power supply, the 8 mm test section was destroyed and replaced by a new one. This also entailed the installation of previously used and new thermocouples, as well as new thermal insulation, along the new test section. Because of a persisting leak, the electrically insulated fitting containing a pressure tap near the downstream end of the new test section was disconnected, which made it impossible to measure the pressure change across the new test section. Moreover, due to miscalculation, the heated length of the new test section turned out to be slightly smaller than that of the old one. Another change in the loop was made in order to reduce the fluid volume in the system: the rod-bundle test section was disconnected.

Finally, the cooling system was altered: the loop is now connected to the university's central chilled water system. A dedicated self-standing chiller using ethylene glycol as coolant is also available, if needed. The main components of the system are described briefly in the following paragraphs.

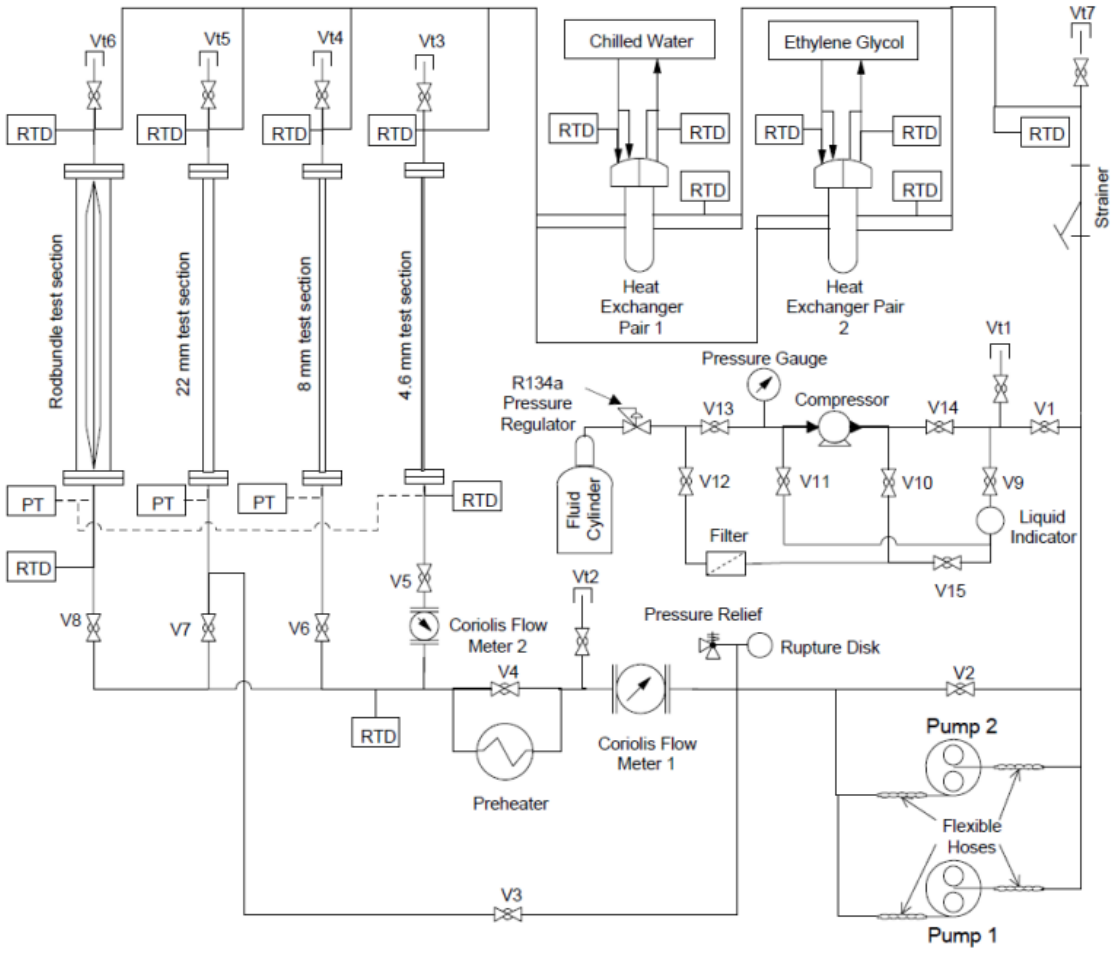

Figure 3.1: Schematic diagram of SCUOL; RTD denotes a resistance temperature detector; PT denotes a pressure transducer; Vx denotes valve x; Vtx denotes vent x.

R134a supply: A low pressure R134a cylinder was used to supply the loop with R134a. While stored in the cylinder, the fluid exists in a liquid state that is both colourless and odourless. According to the supplier's material safety data sheet (MSDS), R134a is non-hazardous at the quantities used in SCUOL. Due to its action as a greenhouse gas, which is much stronger when compared to carbon dioxide, leaking the substance to the atmosphere is prohibited by the federal halocarbon regulations

(Government of Canada, 2022). To prevent this, a leak test of SCUOL must be done annually. In the event of a release of between 10 and 100 kg, the Ontario branch of Environment and Climate Change Canada (ECCC) must be informed within the timelines provided in the regulations. If a release exceeding 100 kg occurs, ECCC must be informed withing 24 hours of the release (Government of Canada, 2022).

Refrigerant recovery unit: The section of the loop to the left of V1 in figure 3.1 is for charging and recovering refrigerant from the loop. The refrigerant recovery unit, labelled as compressor in figure 3.1, provided additional pressure to move the refrigerant from the cylinder to the loop, got the loop up to the required pressure prior to heating, and recovered the refrigerant from the loop back into the R134a cylinder. This section of the loop also includes a liquid indicator as well as a filter to ensure that the refrigerant remained in liquid state and was free of any contaminants.

Pumps: Two gear pumps (Micro Pump Model GL-H23.JFS.E-M2N1CH15) were connected to the loop and used to drive the fluid through the loop at varying flow rates. Figure 3.1 shows their position in the loop, as well as their parallel configuration. To prevent overpressurisation and overheating of the loop, the loop bypass valve V2 was always kept partially open. This ensured that some fluid would always flow through the bypass branch in the event that all the isolation valves were closed.

Preheater: An electrical preheater (CAST-X 3000 circulation heater, part number BX17E6G300U-WTT, Cast Aluminum Solutions, Batavia, Illinois, USA), was used to adjust precisely the test section inlet temperature T_{in}. The preheater is rated for 21.3 kW and has a maximum operating pressure of 17.2 MPa.

Cooling systems: The working fluid is passed through four heat exchangers (Model FXF-6223U, Sentry Equipment Corp, Oconomowoc, Wisconsin, USA), which cool it down to a sufficiently low temperature for each test. The heat exchangers operate in pairs; one pair is configured to be cooled by the university's chilled water system, the other pair is cooled by recirculating ethylene glycol (EG) and a chiller. The EG cooling system was not used for the present work, as the chilled water provided enough cooling capacity for the system's needs.

Pressure regulation: The loop is pressurisied by using the refrigerant recovery unit as a compressor, to move R134a from its cylinder into the test section up to a

maximum pressure of 80 psig. To ensure the volume of refrigerant inside the loop was enough, the room containing the loop was temperature controlled to 18°C. By lowering the temperature of the room a few degrees, it was ensured that more volume of R134a could be compressed into the loop, since the decrease in temperature causes a decrease in pressure per unit volume of the refrigerant. This is advantageous to ensure that boiling does not occur during the start up of the loop. Once test conditions were approaching their desired values, R134a was bled from the loop back into the cylinder to make fine pressure adjustments. Additionally, to dampen pressure fluctuations during operation, the bypass valve V3 connecting the pump outlets straight to the 22 mm test section was partially or fully open. By keeping valves V5, V7, and V8 closed and allowing V3 to act as a throttle for the flow through the unheated test section, the pressure fluctuations were damped.

Test section: An 8 mm internal diameter tube was used as test section (TS) for the present tests. Following failure of the test section used by Mouslim, a new 8 mm test section was installed with the same vertical orientation. This TS has a wall thickness of 1 mm and a heated length of 1,881 mm. The tube material is Inconel® 600 (Special Metals Corporation of Huntington, West Virginia, USA). This material used as has a thermal conductivity that is nearly insensitive to temperature.

Power supply: The TS wall was heated electrically by current supplied from a 3000 A, 60 V power supply. The power supply output is carried by two cables rated at 500 A each and connected to the ends of the TS on machined copper blocks. The copper blocks were coated with a carbon-based grease to keep the contact resistance between them and the 8 mm tube as small as possible. The power supply is connected to the University's 380 V, 60 Hz, 3-phase AC power grid and is rectified to produce a non-negative fluctuating voltage at a frequency of 360 Hz. The thermal inertia of the TS material allows for the wall temperature to remain constant in time.

Safety devices: The room containing the test section is fitted with an oxygen monitoring sensor (Oxyguard®, OxyGuard International A/S, Farum, Denmark) and a high-volume ventilation system. This system works to mitigate any asphyxiation hazard presented by a leak risk of high-pressure R-134a by constantly supplying the room with fresh air. Additionally, to prevent overpressurisation of the test section

in the event of loss of cooling or loss of pump power, a high-pressure relief valve (Swagelok® SS-R4S8, Swagelok Central Ontario, Ontario, Canada) is installed into the loop and set to a maximum pressure of 5.17 MPa (750 PSI).

3.2 Measurement procedures

Temperature measurement: The test section inlet T_{in} and outlet T_{out} temperatures were measured by in-flow RTDs (Omega P-M-1/10-1/8-5-1/2-G-15), having an uncertainty of 0.35 K. The upstream RTD was positioned approximately 2 m before the first power clamp (start of the heated length of the TS) and the downstream RTD was located 0.40 m after the second power clamp. The TS wall temperature $T_i, i = 1, 2, ..., 40$ was measured by 40 T-type thermocouples (TCs), attached to the exterior surface of the TS (OMEGA SA1XL-T-SRTC). The thermocouples have an uncertainty of 0.5 K and a maximum time constant of 0.15 s. The TC axial positions along the TS are listed in table 3.1.

Each TC voltage E was measured by a data acquisition module (National Instruments, Model NI-9217, Austin, Texas, USA) and converted to temperature T by using the following standard relationship for T-type thermocouples (American Society for Testing and Materials, 2011)

$$E = c_o + c_1 T + c_2 T^2 + \cdots + c_8 T^8 \ , \tag{3.1}$$

where E is in volts, T is in degrees Celsius, and the values of the coefficients $c_n, n = 1, 2, \cdots, 8$ are listed in Table 3.2.

Each TC reading was corrected as follows. The loop was operated at a large flow rate without test section heating or preheating, so that it could be assumed that the temperature along the entire TS would be essentially equal to an average room temperature. As figure 3.2a shows, the inlet and outlet RTD readings were nearly identical and the TC readings, averaged over 3 min of sampling, were scattered by fractions of degrees C around the average RTD reading. Each thermocouple reading was offset by the difference between the average RTD reading and the TC reading during the unheated tests. The average offset was 0.047°C and the standard deviation of the offsets was 0.054°C, thus negligible by comparison to the overall measurement

TC Number	Axial Position [m]
1	-0.615
2	-0.359
3	-0.240
4	0.048
5	0.101
6	0.146
7	0.196
8	0.245
9	0.295
10	0.343
11	0.391
12	0.441
13	0.49
14	0.540
15	0.588
16	0.638
17	0.688
18	0.737
19	0.785
20	0.835
20	0.885
22	0.934
23	0.983
24	1.065
25	1.113
26	1.163
27	1.212
28	1.260
29	1.311
30	1.359
31	1.408
32	1.458
33	1.507
34	1.555
35	1.604
36	1.653
37	1.703
38	1.751
39	1.801
40	1.851

Table 3.1: Axial distance of thermocouples from the start of the heated length of the test section.

uncertainty.

In addition to the unheated test, two other tests were performed with the TS unheated, but the inlet temperature raised with the use of the preheater. If the TS

Coefficient	Value
c_0	0.0
c_1	3.874×10^{-2}
c_2	3.329×10^{-5}
c_3	2.062×10^{-7}
c_4	-2.188×10^{-9}
c_5	1.100×10^{-11}
c_6	-3.082×10^{-14}
c_7	4.548×10^{-17}
c_8	-2.751×10^{-20}

Table 3.2: Coefficients for T-type thermocouple response

and surrounding parts of the loop were perfectly insulated thermally, all RTD and TC would have the same readings. However, as Figures 3.2b,c show, there is a measurable difference between the inlet RTD temperature and the TC4 (the first thermocouple after the upstream power clamp) measurement. This was about 2.8°C for an inlet RTD reading $T_{in} = 48.6$°C and increased to about 3.5°C for $T_{in} = 83.7$°C. This drop is attributed to heat losses in the part of the loop between the RTD location and the first power clamp. Such losses would have been also present in all previous tests in SCUOL and would increase with increasing preheating. The downstream RTD reading was lower than that of TC40 (the last TC before the second power clamp) by about 0.5°C for $T_{in} = 48.6$°C and about 1°C for $T_{in} = 83.7$°C. This also indicates some heat losses between the locations of TC40 and the second RTD. Figures 3.2b,c further indicate that there were some heat losses along the heated TS (about 0.25°C for $T_{in} = 48.6$°C and about 0.5°C for $T_{in} = 83.7$°C). The TS and other parts of SCUOL were insulated and, following relocation, we put effort into improving the thermal insulation. Nevertheless, considering the relatively wide ranges of conditions, it seems impractical to estimate corrections for heat losses in the present tests, and even less so to previous tests. Considering that the objectives of the present work are largely qualitative, we will neglect such losses and we will use the RTD readings as nominal inlet and outlet temperatures to the heated TS.

Pressure and mass flux: Pressure measurement was done using a pressure transducer (Omega PX01C1-3KA5T), connected to the inlet of the test section. This

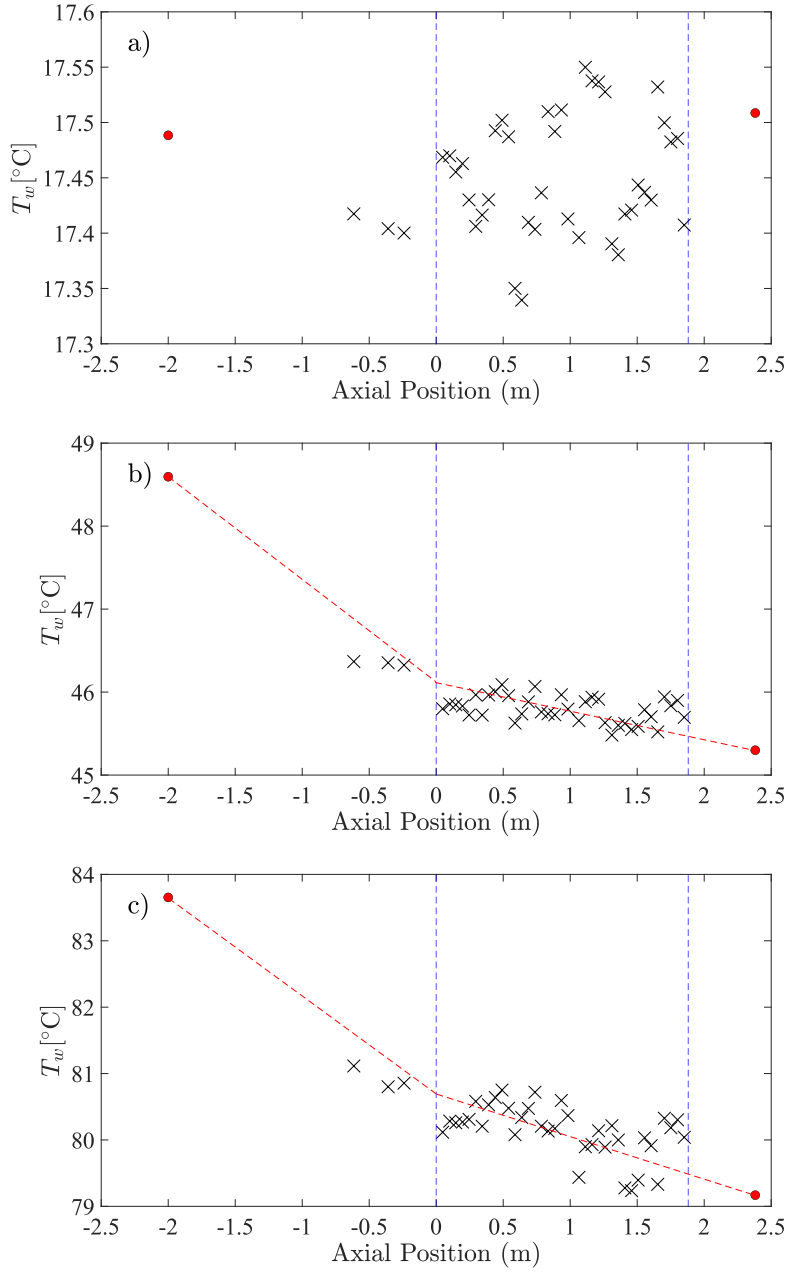

Figure 3.2: Wall temperature along the test section without wall heating. a) Without preheating ($G = 926$ kg/m^2 s). b) With the preheater set at 65 °C ($G = 915$ kg/m^2 s). c) With the preheater set at 105 °C ($G = 753$ kg/m^2 s). Inlet and outlet RTD measurements are shown by red symbols. Vertical dashed lines mark the locations of the upstream and downstream power clamps. Red dashed lines are hand-fitted lines to the data before and after the upstream power clamp.

transducer has an uncertainty of 214 kPa (31 PSI). This pressure was used as the nominal test section pressure. The mass flow rate of the test section was monitored using a Coriolis flow meter (Micro Motion ELITE CFM050M320N0A2E2ZZ), having an uncertainty of 0.05%.

Test section voltage: The test section voltage was measured across the two copper power clamps using a 24-bit, high frequency, digital voltage measurement module (National Instrument NI 9225). The module features a working range of ±300 V with an uncertainty of 0.034 V. Labview was used to process the signal from the module to obtain the RMS voltage across the length of the test section.

Heating power: Heating power is calculated by a program in Labview using the electrical resistance of the test section, as well as the RMS voltage and current. The resistance of the new test section was found using the relation

$$R = \frac{\rho_e L_h}{A}, \tag{3.2}$$

where ρ_e is the electrical resistivity of Inconel provided by the TS manufacturer, L_h is the heated length and A is the cross sectional area of the TS. Values are provided in Table 3.3. The electrical power heating the test section was calculated from the

Table 3.3: TS electrical properties

Test Section Material	ρ_e [µΩ m]	L_h [m]	A_{cs} [m^2]	R [Ω]
Inconel® 600	1.03	1.881	2.827×10^{-5}	0.0681

TS resistance and the RMS voltage V_{RMS} as

$$Q = \frac{V_{RMS}^2}{R}. \tag{3.3}$$

Wall heat flux calculation: Neglecting heat transfer to the surroundings or the unheated portion of the test section, the wall heat flux can be calculated as

$$q = \frac{Q}{\pi d L_h}. \tag{3.4}$$

Inner wall temperature calculation: The temperature of the inside of the test

section wall was estimated from the axisymmetric heat diffusion equation with uniform internal energy generation as

$$T_w = T_{w,o} + \frac{2q_{loss}r_o - q_v r_o^2}{2k} ln\left(\frac{r_o}{r_i}\right) + (r_o^2 - r_i^2)\frac{q_v}{4k}, \tag{3.5}$$

where $T_{w,o}$ is the outer wall temperature, q_{loss} is the heat loss to surroundings (assumed to be zero in the present work), r_o is the outer tube radius, r_i is the inner tube radius, k is the local thermal conductivity of the TS, and q_v is the volumetric heat generation. q_v is calculated as

$$q_v = \frac{Q}{\pi(r_o^2 - r_i^2)L_h}. \tag{3.6}$$

The thermal conductivity k of the test section wall is estimated from the local outer wall temperature using a linear fit (Jiang, 2015) valid in the temperature range from 20°C to 300°C, as specified by the manufacturer

$$k = 0.0146T_{w,o} + 14.509. \tag{3.7}$$

3.3 Operating procedures

Pressure and mass flux control: To reach an adequate pressure for each SC test, the loop was filled with R134a up to the pressure limit of the refrigerant recovery unit, which was 550 kPa (80 PSI). Mass flux was then adjusted using the pump's variable frequency drive (VFD), and the main pump bypass valve V2 (Figure 3.1). By slightly opening and closing the the bypass valve, either less or more fluid was forced to be circulated in the loop through the pumps. Once a steady flow had been established, the preheater and the loop power were turned on to increase the temperature of the loop to the lowest temperature scheduled to be tested that day. As temperature of the loop rises, so does the pressure. When the pressure grew too high before reaching the target temperature, some R134a was bled back into the R134a cylinder to decrease the pressure. Additionally, the temperature could be controlled by throttling the mass flow rate of chilled water being supplied to the heat exchangers. As the temperature in the loop approached the pseudocritical value, the mass flux changed measurably as the heat flux or the inlet temperature were changed. The 8 mm isolation valve

(V6) was operated to provide fine mass flux adjustment as the desired heat flux and inlet temperature were approached.

Heat flux control: The heat flux was controlled by adjusting the power supply's output via the POT dial on the power supply control panel. The heat flux is calculated and displayed in real time by Labview as per equation 3.4. It was ramped up slowly to the target value to prevent TS wall overheating or coolant boiling. Upon changing the heat flux, it took between one and five minutes for the system to reach steady state.

Inlet temperature control: The inlet temperature was controlled to a specific value using the preheater. After the value at the preheater was set, it took $10 - 30$ min for the system to reach steady state.

Recording measured values: Once pressure, mass flux, inlet temperature, and heat flux all reached their target values for the specific test run and steady state was achieved, recording of values began. The recording time for each data set was approximately 180 s, at a sampling rate of 10 Hz, allowing for the collection of approximately 1800 individual readings on all sensors. Measured values were stored in a text file and saved for post-processing.

3.4 Power imbalance considerations

A measure of the overall measurement uncertainty in the present tests is the power imbalance ΔQ, defined as the difference between the heating power Q and the measured enthalpy increase across the test section, namely, as (Mouslim & Tavoularis, 2019)

$$\Delta Q = Q - \dot{m}\left[\left(H_{b,out} + \frac{v_{out}^2}{2} + gz_{h,out}\right) - \left(H_{b,in} + \frac{v_{in}^2}{2} + gz_{h,in}\right)\right] . \tag{3.8}$$

The bulk enthalpy $H_{b,in}$ and other thermophysical properties (density and viscosity) at the inlet can be found from the NIST tables for the measured inlet pressure P and inlet temperature T_{in}, the latter corrected for heat losses in the unheated part of the TS, as estimated from the difference between the reading of the inlet RTD and the first three thermocouples. To determine these properties at the outlet in a similar manner requires values for the outlet pressure and temperature. We may estimate the

outlet temperature from the reading of the outlet RTD, if possible corrected for heat losses beyond the heated TS end. As mentioned previously, however, the current configuration of SCUOL does not permit the measurement of the pressure change across the test section, making it impossible to measure the outlet pressure. As an approximation, we may neglect the pressure change across the TS and use as outlet pressure the value that was measured at the inlet. A rough estimate of the ensuing error may be obtained by estimating the outlet pressure by subtracting the frictional, hydrostatic and acceleration pressure losses from the inlet pressure, as described by Zahlan *et al.* (2014)

$$P_{out} = P_{in} - \frac{f}{2d}\int_0^L \rho_b(z) v_b^2(z) dz - g\int_0^L \rho_b(z) dz - G[v_b(L) - v_b(0)] \ , \tag{3.9}$$

where the average friction factor is estimated from the empirical correlation

$$f = \frac{2.43 Re^{0.26}}{(1.82 \log_{10}(Re) - 1.64)^2} \ . \tag{3.10}$$

As a sample calculation, we determined that the outlet pressure for case 2O1 in table 4.1 ($T_{in} = 77.9°$C, $G = 695.8$ kg/m^{2}s, $q = 85.6$ kW/m^2) dropped by 0.3% from its inlet value. The change in the second term on the right-hand side of equation 3.8 when the corrected outlet pressure was used to calculate the local properties instead of the inlet pressure was about 0.6% (660 Pa). The power imbalance for this test case was calculated to be 3.5 % of the applied power Q when the corrected pressure was used and 4.1 % of Q when the inlet pressure was used. Both of these numbers are comparable to typical power imbalances (within $\pm 5\%$) found by Mouslim (2019). Because the pressure drop was so small, we will neglect its effect on the power imbalance as well as on the values of thermophysical properties determined from the NIST tables.

Chapter 4

Selection of test conditions

In the present study, fluid 1 is CO_2 and fluid 2 is R134a. A few test cases in fluid 1 were selected from the extensive database of Kline & Tavoularis (2017); Kline (2017). This chapter describes the methodology for the selection of test conditions in fluid 2 and lists the thermalhydraulic conditions for the tests, which are determined by adjusting the following settings in SCUOL:

- the pressure of the loop,
- the test section inlet temperature,
- the pump speed, and
- the electric power supplied to the test section.

4.1 Ottawa method

The Ottawa method was applied to scale a set of local fluid conditions in fluid 1 to equivalent local conditions in fluid 2 and to determine the inlet conditions for the fluid 2 tests as follows:

1. The pressure P in fluid 2 was found from equation 2.8. We neglected pressure changes within the test section.
2. The bulk temperature T_b in fluid 2 was found from equation 2.9.

3. The mass flux G in fluid 2 was found from equation 2.10.

4. The wall heat flux q in fluid 2 was found from equation 2.11.

5. The local bulk enthalpy H_b in fluid 2 was found from the NIST tables for the previously found values of pressure and bulk temperature.

6. The inlet bulk enthalpy was calculated from the energy equation as

$$H_{b,in} = H_b - \frac{\dot{Q} z_h}{\dot{m} L_h} \tag{4.1}$$

   where $\dot{Q}$ is the heating power supplied to the test section, z_h is the distance from the start of the heated test section, $\dot{m}$ is the mass flow rate, and L_h is the heated test section length. The choice of z_h for fluid 2 is arbitrary. In this work, we chose z_h to be comparable to the value at the chosen point in the fluid 1 tests.

7. The inlet temperature T_{in} was found from the NIST tables for the previously found inlet bulk enthalpy.

4.2 Pisa method

To apply the Pisa method in order to obtain heat transfer similarity in the two fluids, one needs to determine the operating conditions in fluid 2 as follows:

1. Determine the operating pressure in fluid 2 that is most appropriate for a desired range of dimensionless specific enthalpy in fluid 1. For this pressure, the ratios of Pr/Pr_{pc} for the two fluids in the same range of dimensionless specific enthalpy would be comparable.

2. Determine the inlet temperature for fluid 2. At this temperature, the dimensionless specific enthalpies N_{SPC} at the inlet would be the same for the two fluids.

3. Determine the inlet velocity for fluid 2 so that the inlet Reynolds numbers are equal in both fluids.

4. Determine the heat flux for fluid 2 that produces the same N_{TPC} as that for fluid 1.

4.2.1 Pressure determination

The values of the required thermophysical properties, specific heat, temperature, enthalpy, density, viscosity, and volumetric expansion coefficient, for CO_2 and R134a at each specified pressure and temperature were extracted from the widely used tables NIST REFPROP7 (Lemmon *et al.*, 2002). The data was extracted from the tables and analysed with the use of functions and scripts written in MATLAB R2021a. The pressure for the CO_2 tests was set at $P = 1.13P_c = 8.336$ MPa, whereas the pressure for the R134a tests was determined to ensure that the ratio Pr/Pr_{PC} in fluid 2 most closely matches the one in fluid 1. The steps in this procedure are as follows:

- Select a case from the CO_2 database and extract the required data.
- Determine the range of the dimensionless enthalpy

$$H^* = (H - H_{PC})\beta_{PC}/C_{p,PC} \tag{4.2}$$

  for this CO_2 data set.

- Select an initial pressure for R134a (e.g., $1.13P_c$).
- Determine the temperature range for R134a that yields the same dimensionless enthalpy range as that for CO_2.
- Determine the Prandtl number ratio Pr/Pr_{PC} for each value of h^* for both fluids.
- Curve fit Pr/Pr_{PC} for both the CO_2 and the R134a data. The purpose of fitting a curve is to produce a continuous function that has a value at every dimensionless enthalpy, rather than discrete values. This allows the performance of mathematical operations more conveniently.
- Determine the mean square difference (MSD) e^2 between the curves for the two fluids.

- Repeat this process for different pressures of R134a and select the pressure that minimises the mean square difference.
- Conduct a sensitivity analysis to ensure that an adjustment of the dimensionless enthalpy range does not drastically affect the result.

An example of the fitted Pr/Pr_{PC} curves can be seen in figure 4.1. The fitted lines are very close to the data points, so that no differences can be distinguished in this figure. On the other hand, small differences are visible in figure 4.2, which zooms into the peak regions. These differences can be ignored, because they contribute less than 1% to the mean square difference.

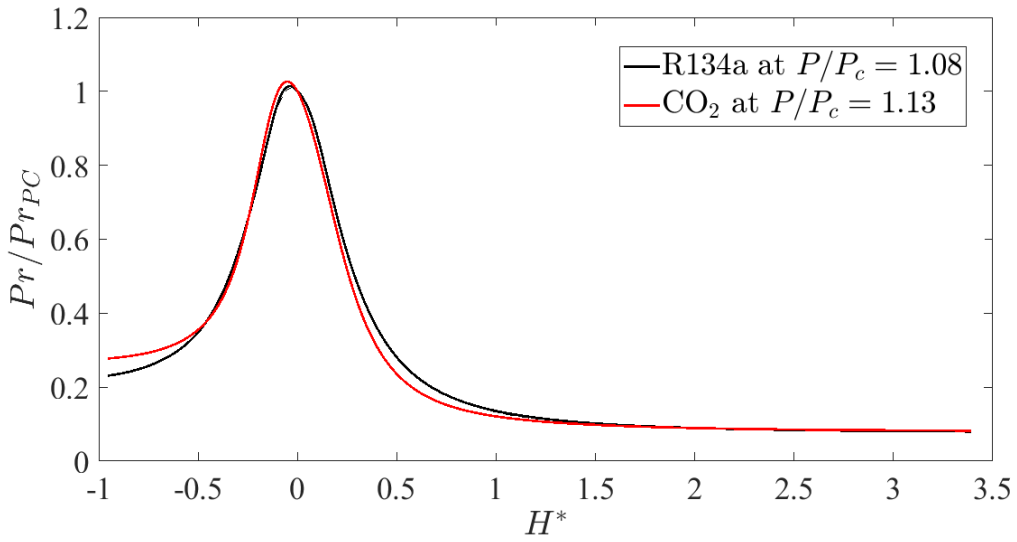

Figure 4.1: Prandtl number ratios for CO_2 at $P/P_c = 1.13$ (red line) and R134a at $P/P_c = 1.08$ (black line) *vs* dimensionless enthalpy.

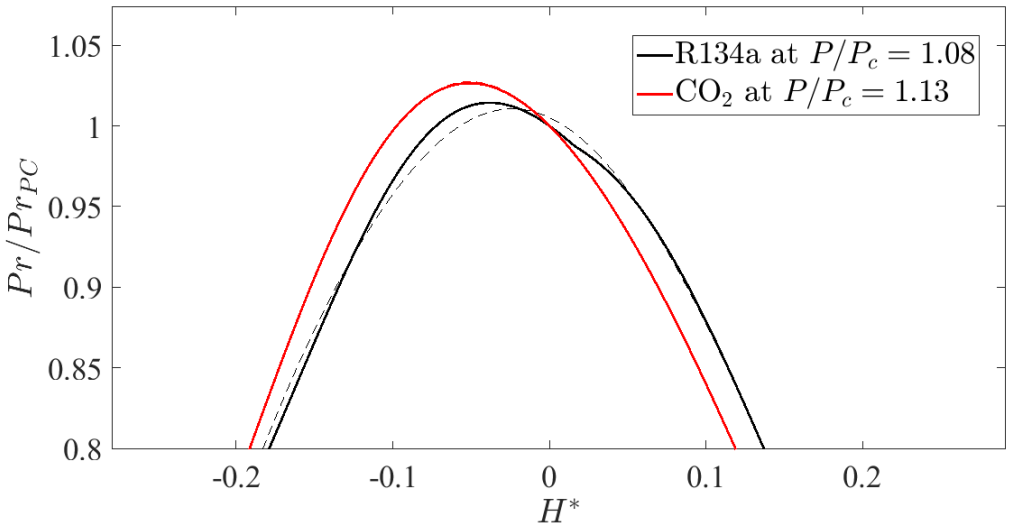

Figure 4.2: Close-up on the peak regions of the Prandtl number ratio for CO_2 at $P/P_c = 1.13$ and R-134a at $P/P_c = 1.08$.

The MSD values, computed over the range $1.05 \leq P/P_c \leq 1.15$, are shown in figure 4.3. A cubic polynomial fits well to the data and shows a minimum at an operating pressure for R134a that can be rounded to $P/P_c = 1.08$.

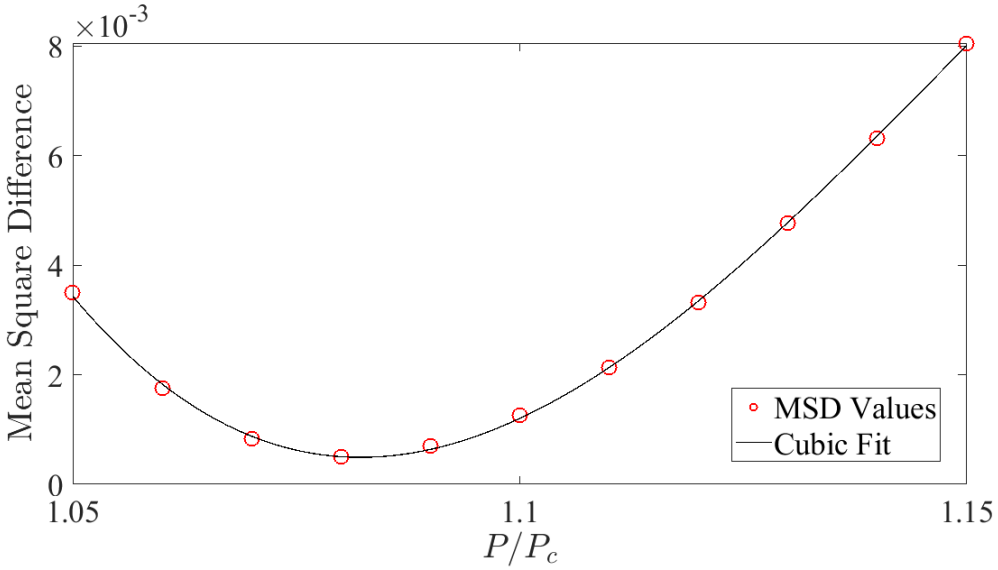

Figure 4.3: Mean square difference between R134a and CO_2 curve fits *vs* P/P_c of R134a.

Before finalising the choice of operating pressure for our tests, we performed some sensitivity analysis to determine whether the chosen pressure is sensitive to the range of dimensionless enthalpy that is taken into account in the MSD calculation. We performed two additional calculations. First, we considered a significantly narrower range of h^*, including regions on either side of the peak, as this is where Pr/Pr_{PC} changes more drastically. Figure 4.4 shows Pr/Pr_{PC} within the narrower enthalpy range and figure 4.5 shows the corresponding MSD for the range of pressures considered. Although the values of MSD increased in magnitude, as the enthalpy range was reduced, the minimum ratio remained close to the previously found value 1.08. As a second sensitivity analysis, we considered a range of dimensionless enthalpy that extended largely to the left of the peak ratio, namely, the liquid-like region. Interest in this region is based on a comment by Pucciarelli & Ambrosini (2020) that, when the specific enthalpy crosses the pseudocritical threshold, the liquid-like region should be considered of greater importance for maintaining similarity, particularly for the onset of DHT. Figure 4.6 shows Pr/Pr_{PC} within this enthalpy range and figure 4.7 shows the corresponding MSD for the range of pressures considered. The MSD values are larger than those in either previous test, yet the minimum MSD shows somewhere between 1.07 and 1.08, close to the previous two results. Thus, the sensitivity tests confirm that the pressure $P/P_c = 1.08$ is approximately the most appropriate one, according to the Pisa method, for tests in R134a to achieve similarity with tests in CO_2 at $P/P_c = 1.13$.

4.2.2 Inlet temperature determination

The procedure for finding the inlet temperature for the test in fluid 2 that has heat transfer similarity with the selected case in fluid 1 is as follows:

- For the selected pressure in fluid 1, determine H_{pc}, β_{pc}, and $C_{p,pc}$ from the NIST tables.
- For the selected pressure and inlet temperature, determine the inlet specific enthalpy H_{in}.
- From equation 2.24, calculate N_{SPC} for fluid 1.

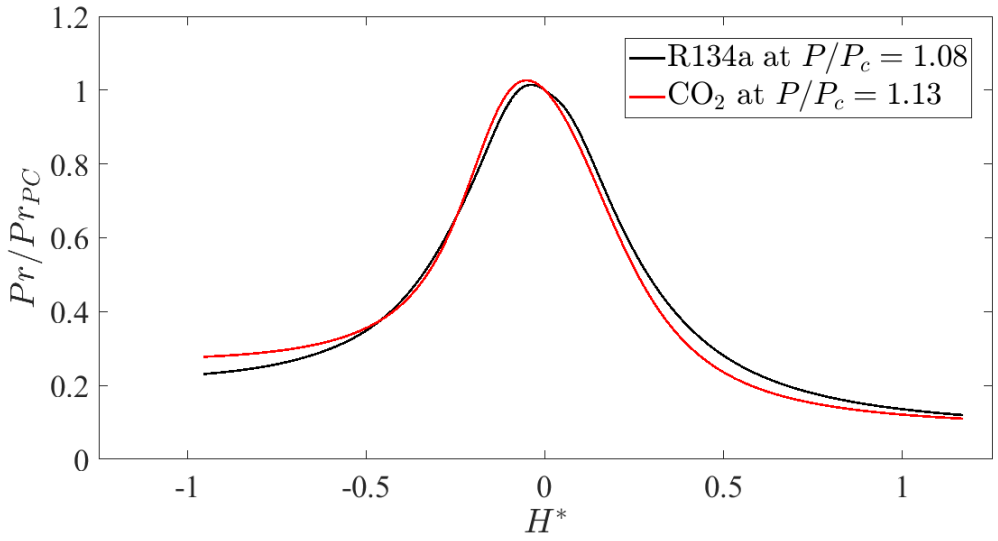

Figure 4.4: Prandtl number ratio *vs* dimensionless Enthalpy between CO_2 at P/P_c = 1.13 and R-134a at P/P_c = 1.08 for a limited dimensionless enthalpy range.

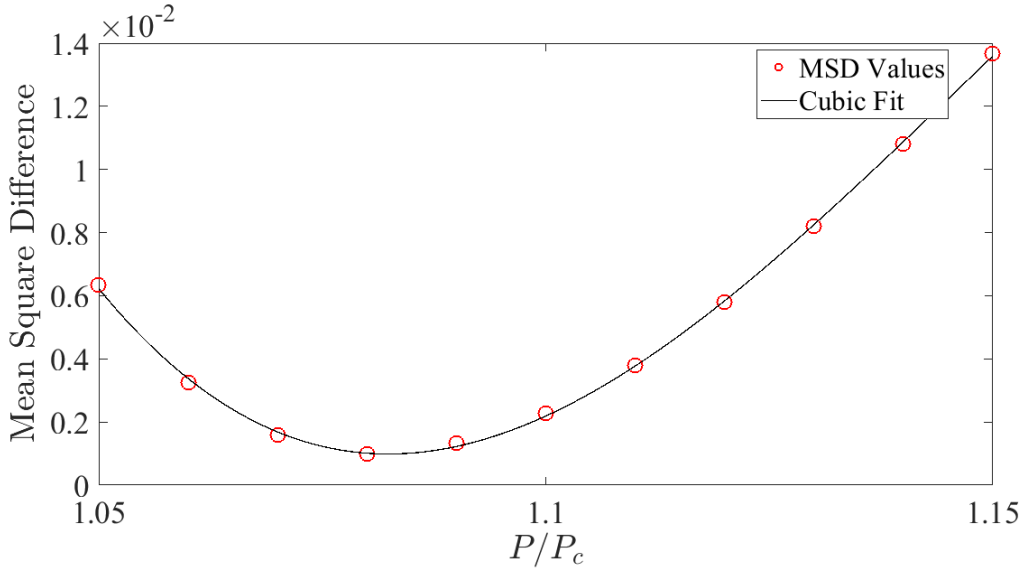

Figure 4.5: Mean square difference between R-134a and CO_2 curve fits *vs* P/P_c of R-134a for a limited dimensionless enthalpy range.

- For the previously found pressure, determine H_{pc}, β_{pc}, and $C_{p,pc}$ for fluid 2.
- Determine N_{SPC} for fluid 2, as equal to its value for fluid 1.
- Using equation 2.24, determine the inlet specific enthalpy H_{in} for fluid 2.

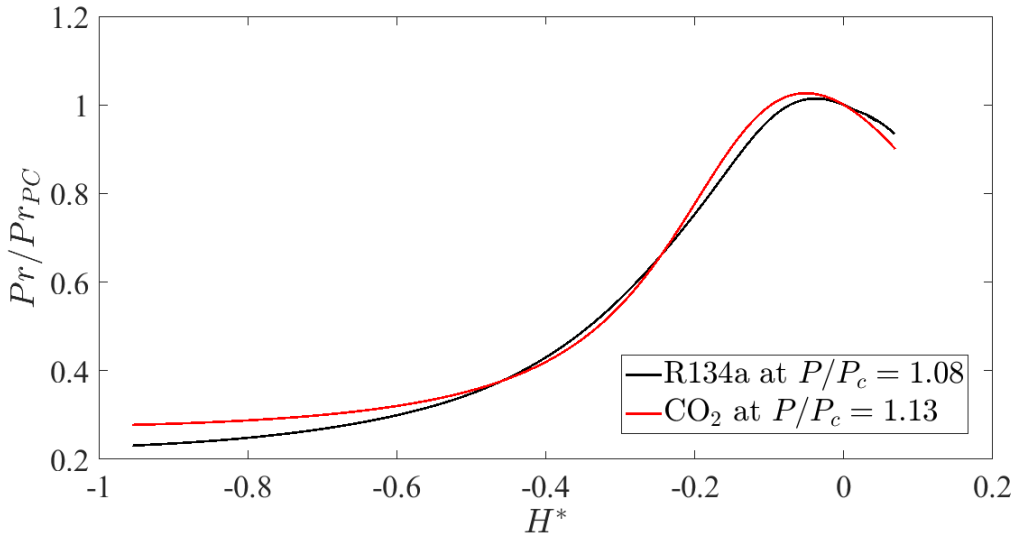

Figure 4.6: Prandtl number ratios for CO_2 at $P/P_c = 1.13$ and R134a at $P/P_c = 1.08$ *vs* dimensionless enthalpy in the liquid-like range.

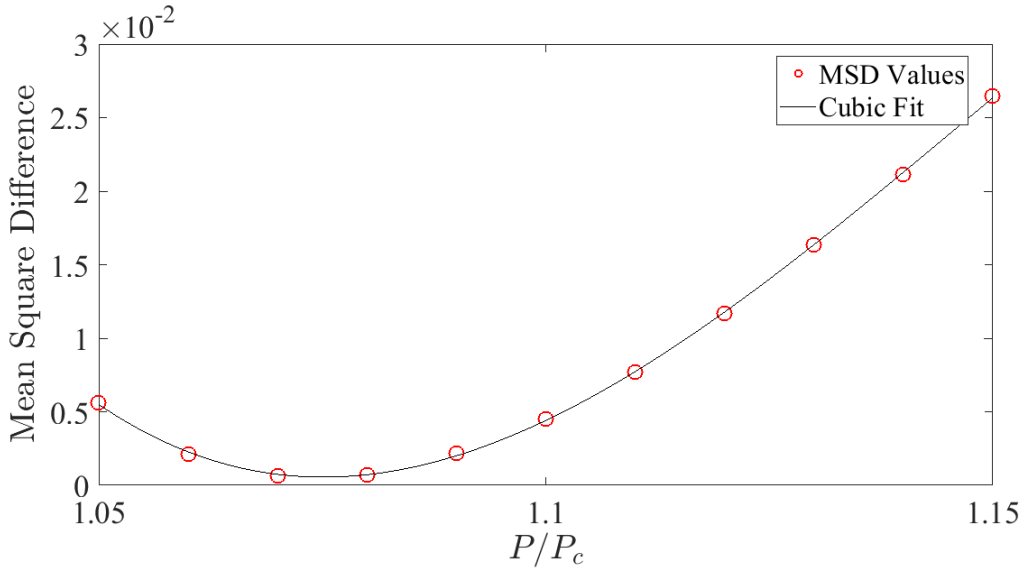

Figure 4.7: Mean square difference between R-134a and CO_2 curve fits *vs* P/P_c of R-134a for the liquid-like dimensionless enthalpy range.

- For this value of H_{in} and the selected pressure, determine the inlet temperature T_{in} for fluid 2 from the NIST tables.

4.2.3 Flow rate determination

The mass flow rate for fluid 2 that corresponds to the selected test for fluid 1 was found as follows:

- From the specified mass flux G and inlet temperature for fluid 1, determine the inlet Reynolds number as $Re_{in} = Gd/\mu$.
- Determine the inlet Reynolds number for fluid 2 as equal to the previously found value for fluid 1.
- Using the Reynolds number and inlet temperature values, determine the mass flux for fluid 2.
- Determine the inlet velocity and the mass flow rate for the given tube diameter.

Ideally, this procedure should also require a change in pipe diameter from fluid 1 to fluid 2 to allow the preservation of the Froude number. As mentioned previously, however, changing pipe diameter multiple times is not possible in experimental tests.

4.2.4 Heat flux

The heat flux for the fluid 2 tests was determined as follows:

- Determine N_{TPC} for the selected test case in fluid 1 using equation 2.18.
- Set the same value of N_{TPC} for a test in fluid 2.
- From the previous value determine a value for the heat flux q.

4.3 Test matrix

Seven reference cases from Kline's dataset have been chosen to scale in the present work. These four cases provided twenty two sets of initial conditions to be tested, seven using the Pisa method, and fifteen using the Ottawa method. The selected ranges of inlet temperature, flow rate, and heat flux were based on two main criteria. First, they are all cases of DHT. It is important to be able to predict DHT, so any

working fluid-to-fluid similarity theory must be able to scale cases where DHT is present. The definition of similarity from Pucciarelli & Ambrosini (2020) states that the spatial distribution of dimensionless enthalpy for the two flows must be the same all along the channel, regardless of heat transfer mode. Therefore, if the reference case contains DHT, the simulant case must have a DHT regime as well to be considered similar. The second reason for this selection is that some of these cases were already scaled by Mouslim (2019) using the Ottawa method. So an investigation was carried out to further look into how the point selected for scaling influences the results.

The initial conditions shown in Table 4.1 were scaled using programs coded in MATLAB to take Kline's data as an input and return the corresponding conditions in R134a according to the Ottawa and Pisa scaling methods.

CO_2 Results	Ottawa-scaled Tests	Pisa-scaled Tests
1: $T_{in} = 14.9$ $G = 400.7$ $q = 35.4$ (K170)	1O1: $T_{in} = 81.0, G = 399.9, q = 26.6$ 1O2: $T_{in} = 81.8, G = 411.7, q = 26.7$ 1O3: $T_{in} = 81.6, G = 421.4, q = 27.4$ 1O4: $T_{in} = 82.5, G = 435.2, q = 27.5$ 1O5: $T_{in} = 82.8, G = 471.6, q = 28.6$	1P: $T_{in} = 88.8$ $G = 403.7$ $q = 19.4$
2: $T_{in} = 12.1$ $G = 700.9$ $q = 115.1$ (K191, M192, M196)	2O1: $T_{in} = 77.9, G = 695.8, q = 85.6$	2P: $T_{in} = 86.6$ $G = 698.5$ $q = 62.9$
3: $T_{in} = 12.1$ $G = 597.9$ $q = 80.4$ (K181, M186)	3O1: $T_{in} = 78.5, G = 618.3, q = 61.2$	3P: $T_{in} = 86.6$ $G = 597.9$ $q = 43.8$
4: $T_{in} = 11.9$ $G = 702.0$ $q = 100.4$ (K188)	4O1: $T_{in} = 78.1, G = 728.7, q = 80.9$	4P: N/A
5: $T_{in} = 14.4$ $G = 701.5$ $q = 120.1$ (K192, M193)	5O1: $T_{in} = 80.5, G = 704.3, q = 90.3$ 5O2: $T_{in} = 81.8, G = 837.0, q = 96.4$ 5O3: $T_{in} = 80.3, G = 695.7, q = 53.2$ 5O4: $T_{in} = 81.7, G = 820.1, q = 72.6$ 5O5: $T_{in} = 82.0, G = 828.2, q = 81.0$	5P: $T_{in} = 86.6$ $G = 703.5$ $q = 66.2$
6: $T_{in} = 10.4$ $G = 700.6$ $q = 105.1$ (K191, M194, M195, MT5)	6O1: $T_{in} = 76.3, G = 718.4, q = 80.2$ 6O2: $T_{in} = 77.7, G = 800.7, q = 84.3$ 6O3: $T_{in} = 78.0, G = 838.0, q = 84.5$	6P: $T_{in} = 85.5$ $G = 693.3$ $q = 57.1$
7: $T_{in} = 9.6$ $G = 702.1$ $q = 98.0$ (K187)	N/A	7P1: $T_{in} = 84.9$ $G = 691.8$ $q = 52.9$ 7P2: $T_{in} = 84.9$ $G = 691.8$ $q = 47.1$

Table 4.1: Experimental conditions for the CO_2 tests considered and corresponding present R134a tests. For all CO_2 and Ottawa-scaled tests, $P/P_c = 1.13$, whereas, for all Pisa-scaled tests, $P/P_c = 1.08$. T_{in} is in degrees C, G is in kg/m^{2}s, q is in kW/m^2. Kxxx indicates page number in Kline's thesis, Mxxx indicates page number in Mouslim's thesis and MT5 indicates Figure 5 in Mouslim & Tavoularis (2019).

Chapter 5

Results and discussion

5.1 Preliminary considerations and tests

In this chapter, we will present original heat transfer measurements in vertical upward flows of R134a in a circular tube under supercritical pressures and analyse these and previously acquired data in CO_2 and R134a to further evaluate the Ottawa and Pisa fluid-to-fluid scaling methods, particularly under DHT conditions. Two types of evaluations will be presented, first a qualitative one, based on the detection or not of DHT anywhere along a wall temperature profile in a scaled R134a test, and second a quantitative one, based on a comparison of Nusselt number values in corresponding CO_2 and R134a tests. The qualitative evaluation was necessitated by the fact that multiple DHT mechanisms may be activated in different fluids under different conditions and that no pair of fluids would have thermophysical properties with identical behaviours, so that perfect dynamic similarity cannot be expected to occur under any conditions. The chosen qualitative criterion is expressed as follows: is a scaling method successful in predicting that, when one fluid exhibits NHT in the entirety of the channel, so will the other, and furthermore that, when one fluid exhibits DHT in some part of the channel, so will the other? In other words, a method will not satisfy our qualitative criterion, if it cannot separate cases with NHT from those with DHT along the channel, irrespective of whether its prediction of heat transfer coefficient is accurate or not. The success of any test of a scaling method is intimately connected to

the soundness of the adopted DHT detection criterion. Among the several suggested criteria for DHT detection, we followed the approach adopted by Kline *et al.* (2018), namely that DHT occurs in sections of the channel, where there is a peak (or bump) in the wall temperature axial profile. This is a local identification of DHT and it seems to be possible for heat transfer to revert to the normal state downstream of a wall temperature peak. Kline *et al.* (2018) were able to verify the occurrence of mild DHT by comparing measured axial profiles of the Nusselt number and corresponding profiles determined from empirical relationships for NHT, but, to avoid possible ambiguities, we only chose to scale CO_2 cases with unquestionably strong local DHT.

A few preliminary tests were first performed to examine the reproducibility of results for NHT cases by comparison to previous (Mouslim, 2019) results. The conditions for three such cases are listed in Table 5.1 and the wall temperature profiles for these cases are shown in Figure 5.1. Both the present and the previous tests indicate NHT and show monotonic increases of wall temperature. The corresponding wall temperature values differ by a few degrees, with a maximum of up to about 10°C, which occurred towards the downstream end of the TS for case c. Such differences exceed the uncertainty of the temperature measurement system and so they must be attributed to other causes. Perfect agreement was hardly to be expected, in view of changes made in the test section, thermocouple sensors and their mounting procedure, insulation, and data acquisition modules. Moreover, as will be discussed in a following section, the measured values were sensitive to the history of settings by which each set of conditions was reached. Considering the mainly qualitative objective of the present study, we may assess that the observed differences are not prohibitive for comparisons between the present and previous results.

Present Tests	Mouslim's Tests
a) $T_{in} = 62$, $G = 1506$, $q = 92$	$T_{in} = 62$, $G = 1488$, $q = 93$
b) $T_{in} = 74$, $G = 1516$, $q = 76$	$T_{in} = 74$, $G = 1519$, $q = 76$
c) $T_{in} = 73$, $G = 1576$, $q = 116$	$T_{in} = 73$, $G = 1575$, $q = 116$

Table 5.1: Experimental conditions for three present preliminary NHT tests and tests by Mouslim (2019) under nominally identical conditions. $P/P_c = 1.13$, T_{in} is in degrees C, G is in kg/m^{2}s, q is in kW/m^2.

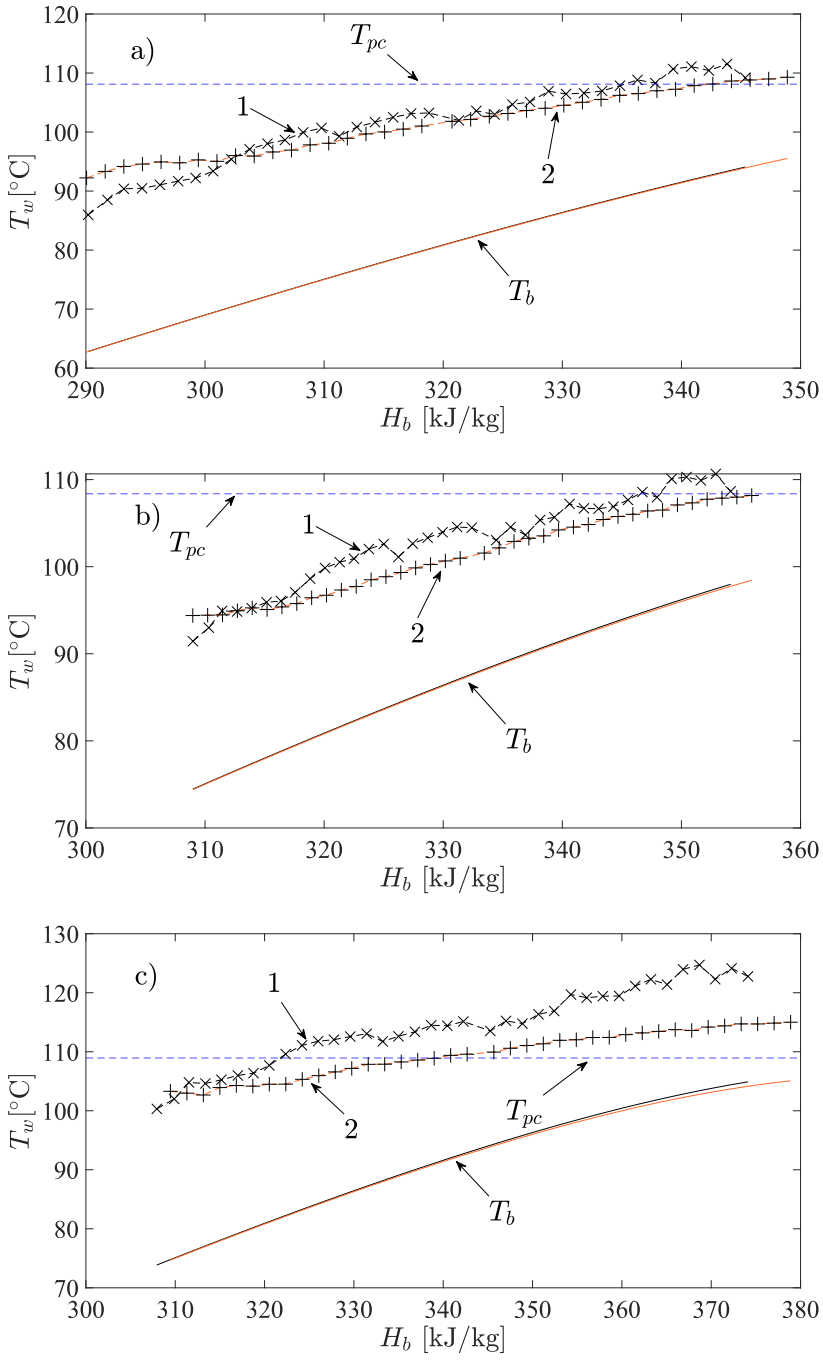

Figure 5.1: Wall temperature profiles in present R134a tests (marked by 1 in the plots) and in tests by Mouslim (2019) (marked by 2 in the plots) under nominally identical inlet conditions, listed in Table 5.1.

5.2 Wall temperature profiles

Selected wall temperature profiles in CO_2, measured by Kline (2017) (see also Kline & Tavoularis (2021)), and presently measured wall temperature profiles in R134a, scaled by the Ottawa and Pisa methods, are shown in Figures 5.2-5.8. The test conditions are listed in Table 4.1. To test the Ottawa method, we scaled points in CO_2 that were both on and off wall temperature peaks and repeated Mouslim's tests that did not follow the pattern of his other results (Mouslim & Tavoularis, 2019). To test the Pisa method, we also scaled different CO_2 profiles, both in NHT and DHT, and examined whether the same mode was observed in the overall R134a profile. We further examined the sensitivity of DHT occurrence upon the imposed wall heat flux and the possibility of DHT onset hysteresis.

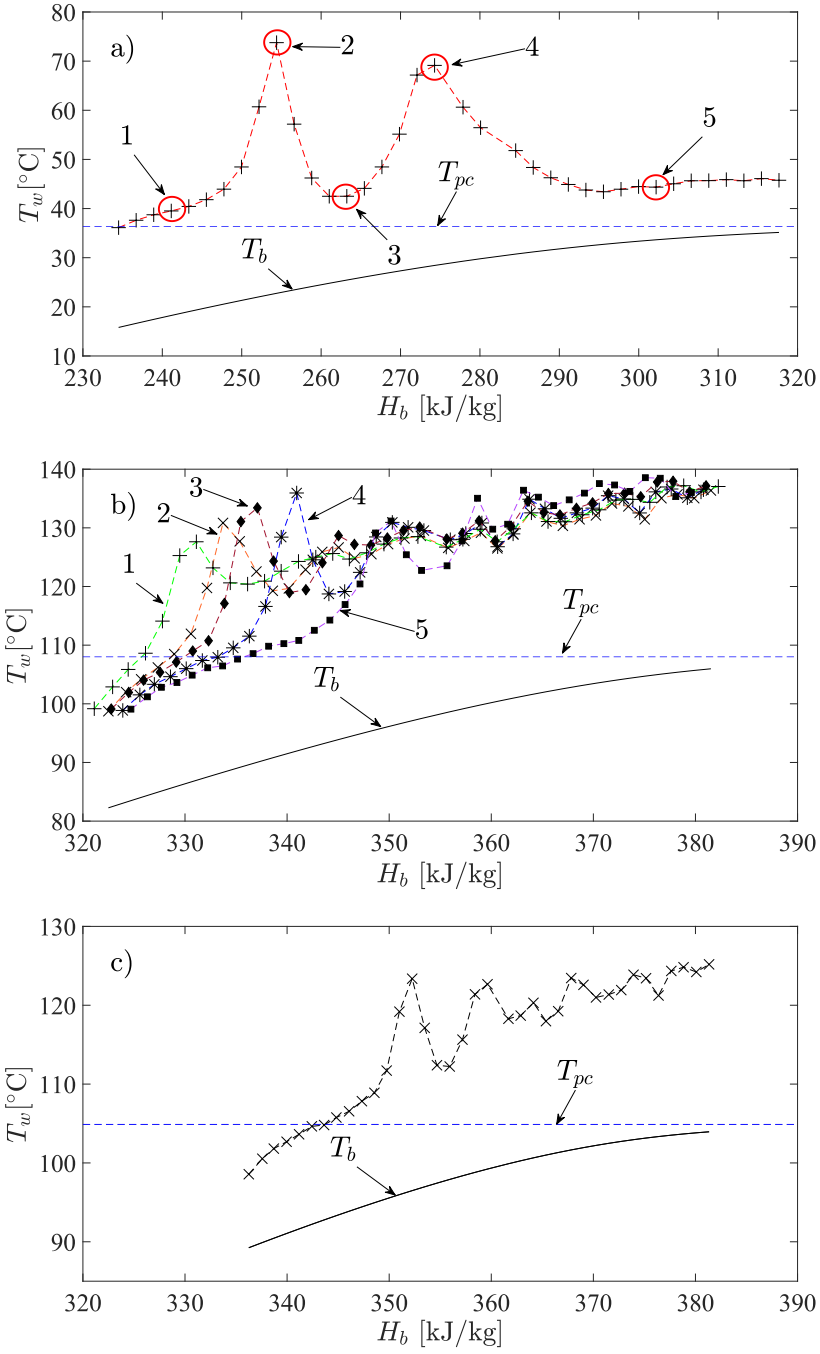

Figure 5.2: Wall temperature along the 8 mm tube containing a) CO_2; b) R134a scaled with the Ottawa method, and c) R134a scaled with the Pisa method. Test conditions are listed in Table 4.1, case 1. In this and following figures, T_b was calculated from the energy equation.

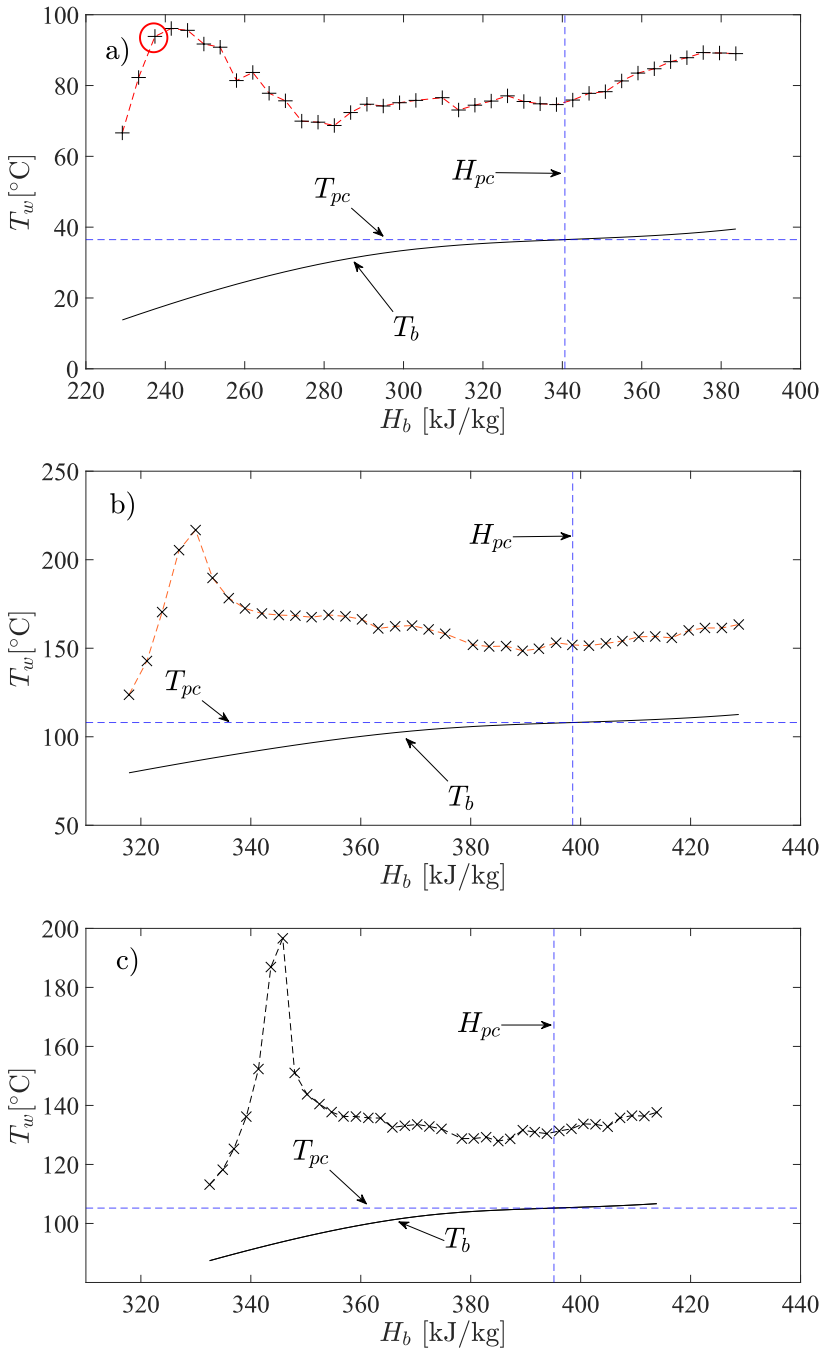

Figure 5.3: Wall temperature along the 8 mm tube containing a) CO_2; b) R134a scaled with the Ottawa method, and c) R134a scaled with the Pisa method. Test conditions are listed in Table 4.1, case 2.

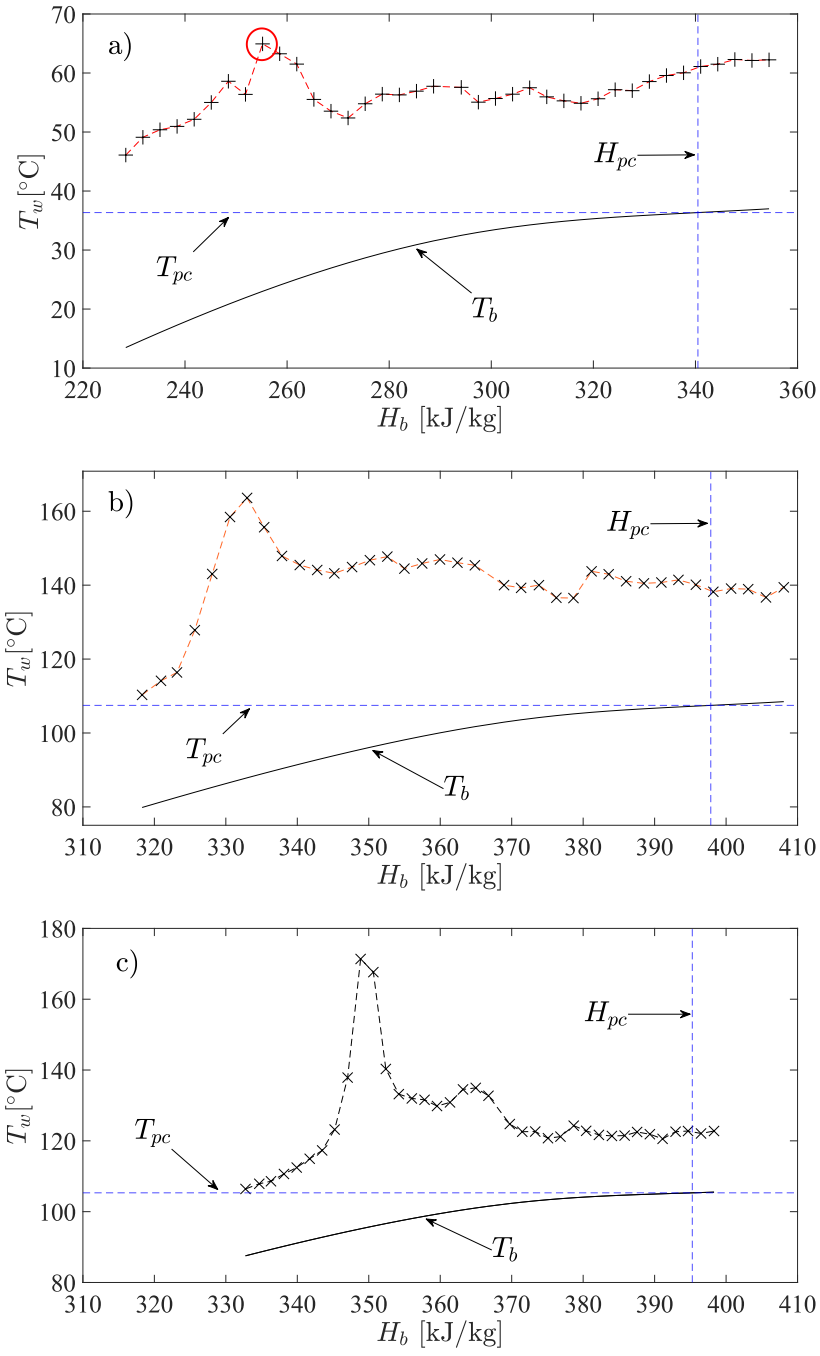

Figure 5.4: Wall temperature along the 8 mm tube containing a) CO_2; b) R134a scaled with the Ottawa method, and c) R134a scaled with the Pisa method. Test conditions are listed in Table 4.1, case 3.

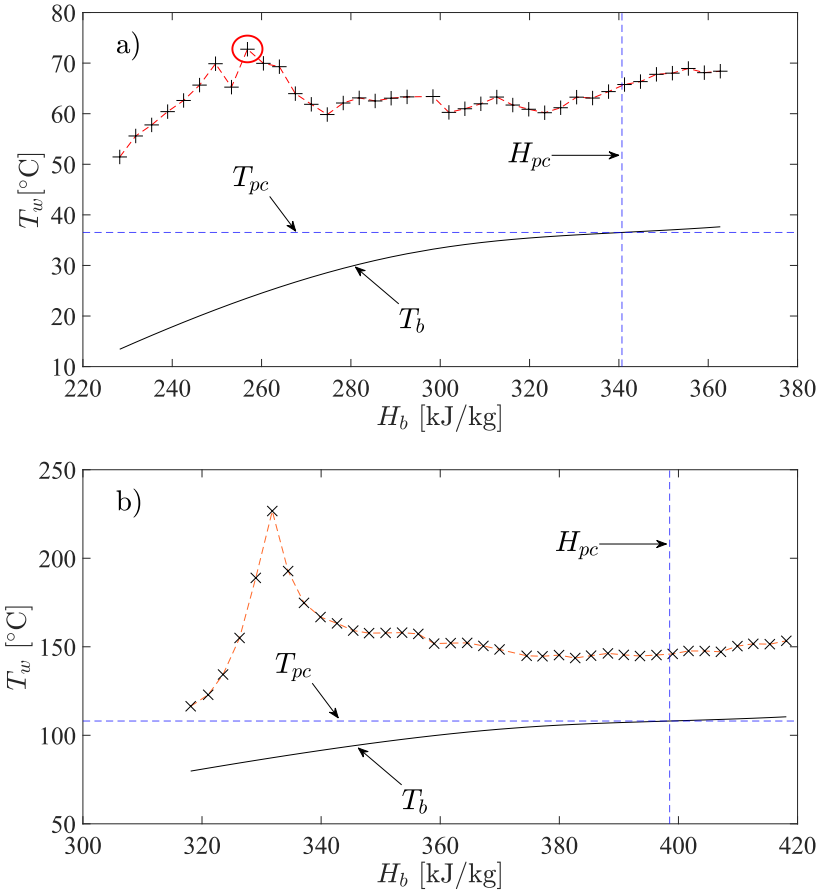

Figure 5.5: Wall temperature along the 8 mm tube containing a) CO_2 and b) R134a scaled with the Ottawa method. Test conditions are listed in Table 4.1, case 4.

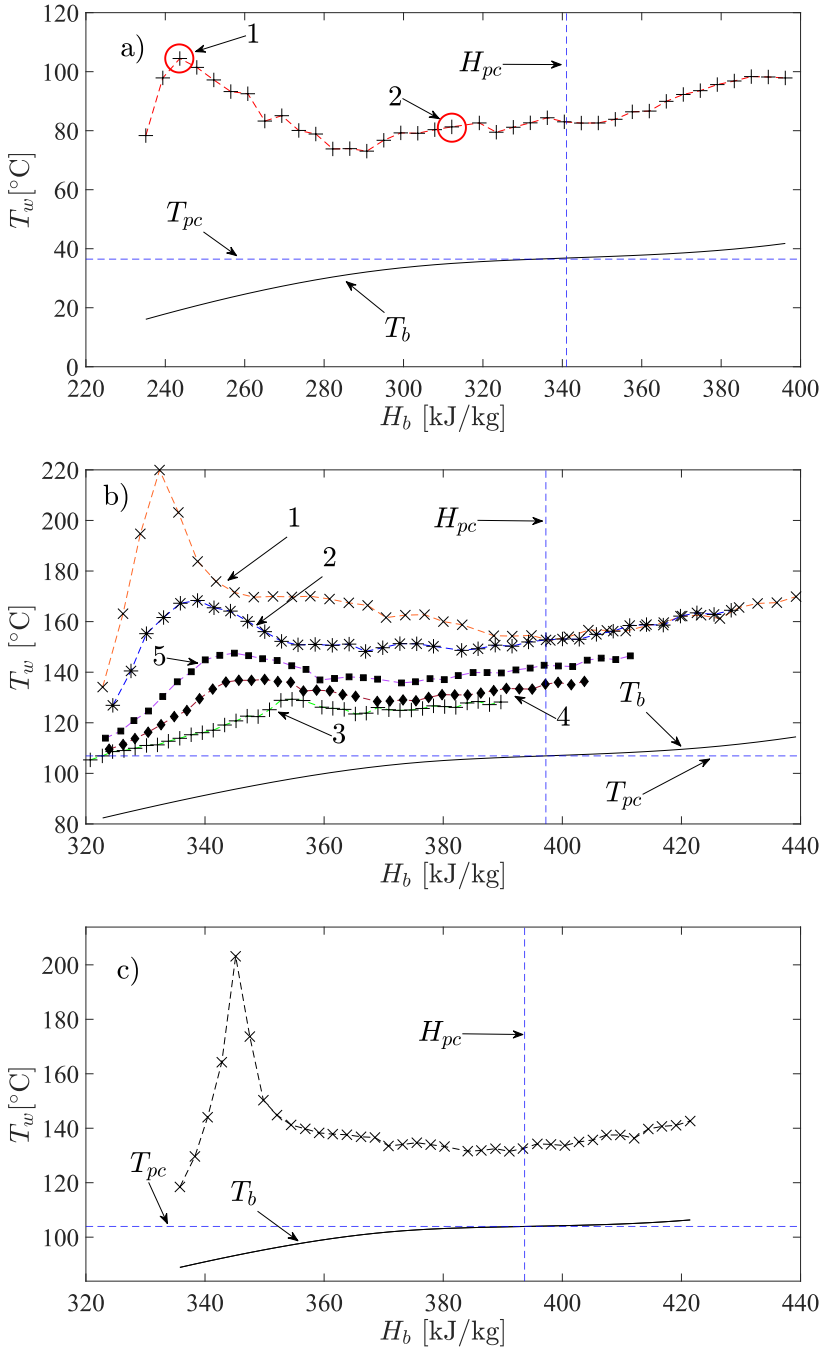

Figure 5.6: Wall temperature along the 8 mm tube containing a) CO_2; b) R134a scaled with the Ottawa method, and c) R134a scaled with the Pisa method. Test conditions are listed in Table 4.1, case 5.

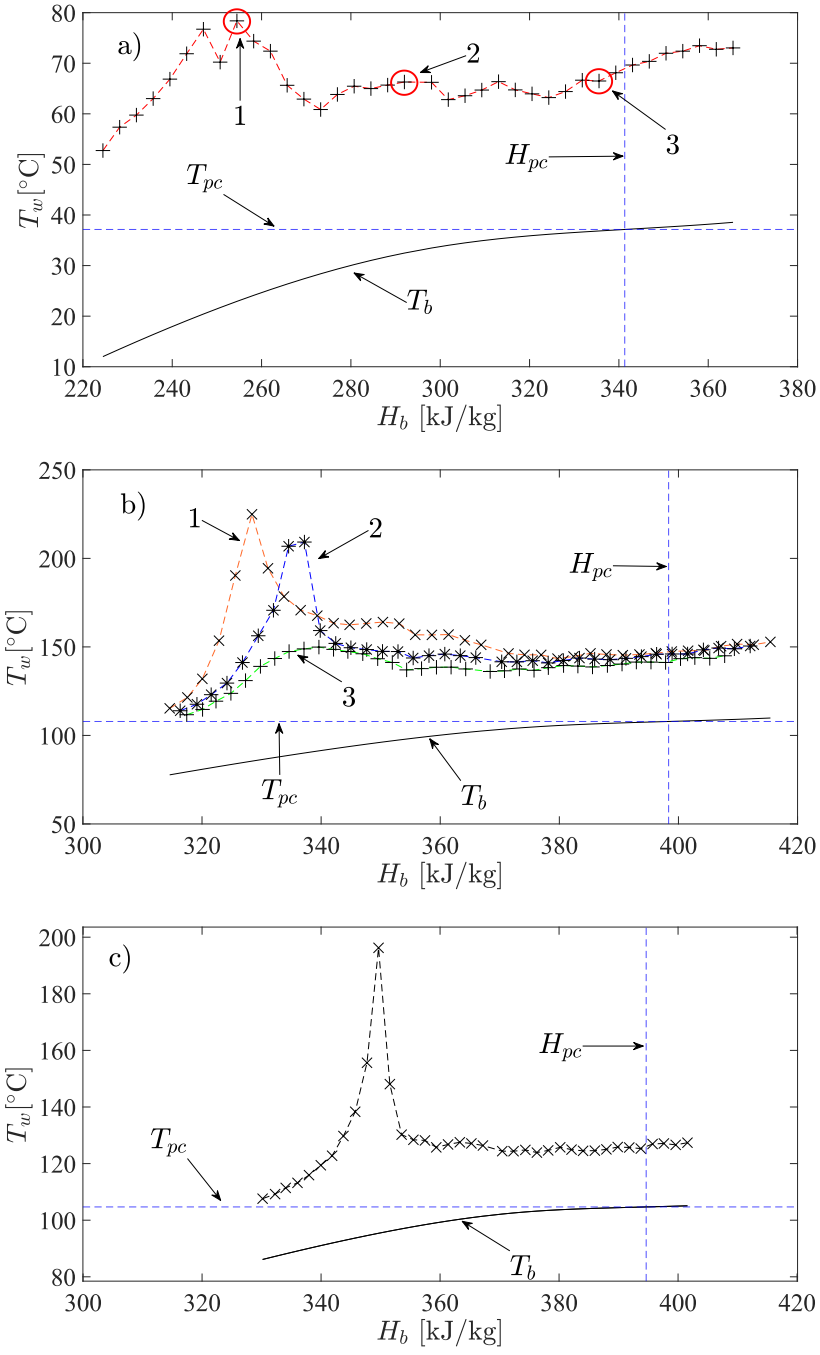

Figure 5.7: Wall temperature along the 8 mm tube containing a) CO_2; b) R134a scaled with the Ottawa method, and c) R134a scaled with the Pisa method. Test conditions are listed in Table 4.1, case 6.

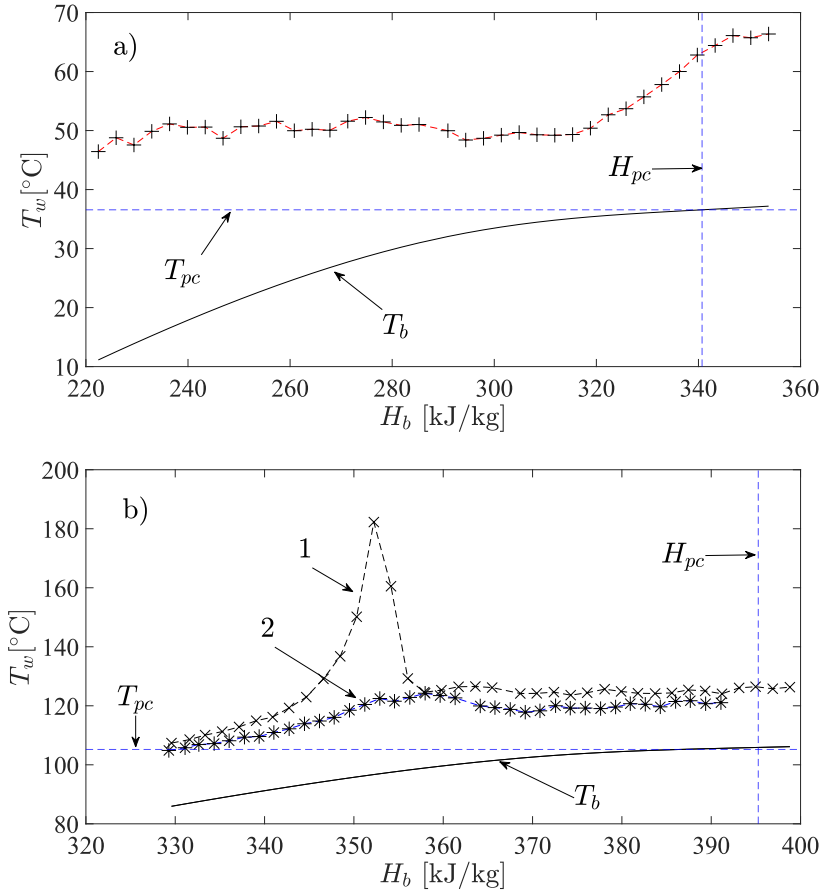

Figure 5.8: Wall temperature along the 8 mm tube containing a) CO_2 and b) R134a scaled with the Pisa method. Test conditions are listed in Table 4.1, case 7.

5.2.1 Ottawa-method scaling

The Ottawa method is based on the scaling of local conditions, an important consequence of which is that the inlet conditions in a R134a test depend on the location of the chosen point in the corresponding CO_2 test. To explore this matter, we show in Figure 5.9 the dependence of the inlet conditions in R134a tests upon the chosen CO_2 point location. One is reminded that the pressure is independent of the chosen point. The pseudocritical bulk enthalpy for this test was 397 kJ/kg, thus above the range of the plot axis. The mass flux increases (up to 19%) as the chosen point is moved in most of the channel, which tends to prolong the occurrence of NHT in R134a. This is the result of a faster increase in the Prandtl number than in the viscosity. This effect is counteracted by an increase in heat flux (up to 9%), which enhances the onset of DHT in R134a. The increase in heat flux is the result of an increase in the bulk thermal conductivity ratio, which is nonlinear and tends to be milder at higher enthalpies. The ratio G/q generally increases as the chosen point is moved downstream, which is also consistent with the tendency to delay or prevent DHT onset. The inlet temperature increases but mildly enough (by roughly 2°C) for its effect to be of secondary importance. It is noted that the values of the R134a inlet conditions are coupled to each other. For example, all G, q and T_{in} peak near the downstream end of the TS. The detailed shapes of these properties are specific to the case considered here and one should avoid generalising the previous observations.

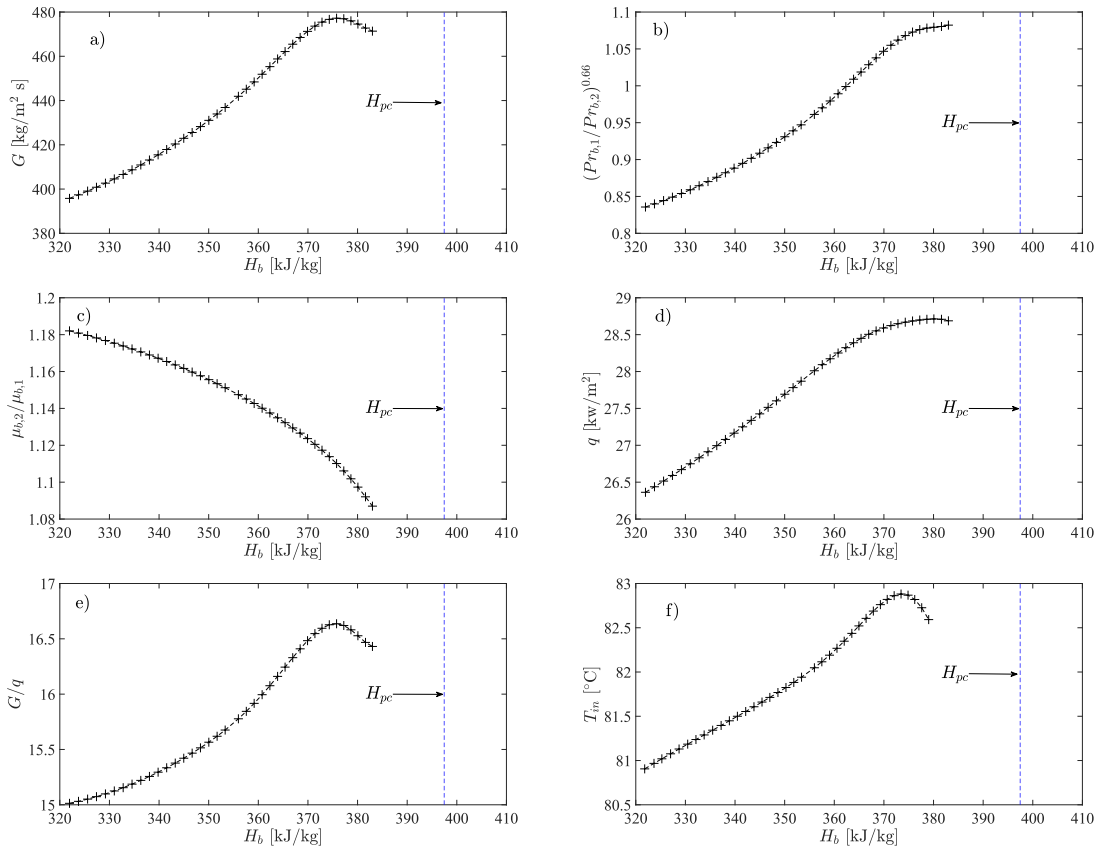

Figure 5.9: Dependence of the calculated a) mass flux, b) Prandtl number ratio, c) dynamic viscosity ratio, d) heat flux, e) ratio of mass flux and heat flux, and f) inlet temperature in a R134a test, scaled with the Ottawa method, upon the location of the chosen point in the CO_2 tests shown in figure 5.2 (conditions listed in Table 4.1, case 1).

Figure 5.2 shows a case with a double peak in the CO_2 wall temperature profile, which is deemed to be clear evidence for DHT. This case has not been considered by Mouslim (2019). We scaled five points: one upstream of both peaks, one on the first peak, one between the peaks, one on the second peak and one well downstream of both peaks. In all cases, the scaled R134a wall temperature profile also had a prominent first peak, followed by additional peaks with diminishing amplitudes. It is also noted that the main peak for the last point was lower than the main peaks for the other points; this introduces the possibility that the R134a profile might be entirely in NHT, if the test section were longer and the chosen point in the CO_2 profile were

moved farther downstream.

The success of DHT scaling from CO_2 to R134a by the Ottawa method appears to be supported by some results of Mouslim (2019) but contradicted by some others. For the reader's convenience, we reproduced the relevant figures from Mouslim's thesis in the Appendix. To begin with, consider case 2 in Table 4.1, which refers to a CO_2 test with clear DHT and corresponds to Figures E.1 and E.5 in Mouslim (2019). In Figure E.1, in which the selected point in the CO_2 test was remotely downstream from the peak, the wall temperature profile in R134a was under NHT. In contrast, in Figure E.5, in which the selected three points were on or near the peak, the R134a profiles were under DHT. We conducted a test under conditions that nominally matched the conditions in Mouslim's tests, selecting a point in CO_2 that was on the peak. Figure 5.3 shows that DHT occurred in our test as well, in conformity with Mouslim's Figure E.5. To ensure that this case is not exceptional, we conducted three additional tests (cases 3, 4 and 5 in Table 4.1), in all of which the CO_2 profiles had a distinct peak, selecting points that were on the peak. As Figures 5.4 and 5.5 show, in cases 3 and 4, the R134a profiles were under DHT. It is noted that case 3 corresponds to Figure D.21 in Mouslim's thesis but he selected the point in CO_2 far downstream of the peak and found the R134a profile to have no peak. For lack of additional information, one cannot deduce whether NHT would have persisted in Mouslim's test, if he had selected a point on or near the peak.

A situation similar to that in case 3 occurred in case 5, shown in figure 5.6. Mouslim (Figure E.2) scaled a point in CO_2 far downstream of the peak and found that the R134a profile had no peaks. We repeated this test for the same point under nominally identical conditions (case 5O2) and found that the R134a profile had a distinct peak, which contradicts Mouslim's finding. We further examined case 5 by scaling a point on the peak of the CO_2 profile (case 5O1) and found that the R134a profile had a peak that was significantly higher and sharper than that in case 5O2. Therefore, both our tests for case 5 show DHT, but, for the case corresponding to a point on the peak, DHT was more intense than that corresponding to a point far downstream of the peak.

To further investigate the conditions that separate NHT and DHT, we performed

three more tests for case 5. For case 5O3, G and T_{in} were set to the same values as for case 5O1, but the heat flux q was increased gradually from zero until DHT was observed. As heat flux increased, the pressure in the test section increased as well, so some R134a had to be bled back into the cylinder to maintain the desired pressure. For case 5O4, G and T_{in} were the same as for case 5O2, but this time q was increased until strong DHT was observed, and then decreased until DHT strength began to decrease noticeably, which indicated a change towards NHT. The pressure in case 5O4 was 4.5% lower than the pressure in cases 5O1 and 5O2. The difference in q between between cases 5O1 and 5O3, which was 52%, was much larger than the difference in q between cases 5O2 and 5O4, which was 29%. This indicates that the strength of DHT in R134a when the scaling point was on the CO_2 peak was significantly higher than that when the point was far downstream of the peak. Additionally, these results show that the thresholds of conditions at the onset of DHT span ranges rather than being sharp and likely depend on the methodology and the history of condition settings. It is important to note that, although pressure could be maintained fairly constant by bleeding R134a while increasing the heat flux, this was not possible while decreasing the heat flux because there is no way of adding more R134a while the loop was running. The full collapse of the peak to NHT in the profile for case 5O4 was observed for q in the vicinity of 60 kW/m^2, but measurements are not reported for this case because the loop pressure had dropped substantially. Because the thermodynamic properties of a fluid depend on pressure, it is expected that a significant change in pressure would also affect the onset of DHT. As the pressure decreases at a fixed temperature, so do the density and the dynamic viscosity, whereas the specific enthalpy increases and the thermal conductivity, the volume expansivity, and the Prandtl number may increase or decrease depending on the temperature value (see Figures 2.3 to 2.16). The direction of DHT onset shift as pressure changes is not easy to determine by intuitive arguments and would likely depend on the fluid and conditions.

As for case 5O4, we examined case 5O5 by maintaining the values of G and T_{in} approximately equal to those for case 5O2, but this time increasing q from a low value at which NHT occurred until noticeable DHT was present. As q was being increased,

pressure tended to increase as well, but it was adjusted to the desired value by bleeding R134a from the loop. The main purpose of this test was to contrast case 5O4 for which q was decreased and thus investigate the possible presence of hysteresis for the DHT onset. It is noted that Kline (2017) and Mouslim (2019) did not address the hysteresis effect because they only performed tests in a sequence of increasing heat flux to avoid recharging the loop with fluid. We found that, in case 5O4, as q was decreased from a large value, DHT switched to NHT at a significantly lower threshold than the value at which NHT switched to DHT as q was increased in case 5O5. In both 5O4 and 5O5, the mass flow rate and inlet temperature were kept essentially constant, but the pressure decreased by about 4.5% from the previous cases. One may argue that repeated measurements may help to confirm claims of hysteresis. Although there are no results presented showing repeated runs, during the process of setting up for data collection, many parameters had to be finely changed before reaching desired test conditions. The parameters were often overshooting, then undershooting, sometimes multiple times, the desired test values. It was observed during this process that there was repeatability in wall temperature profiles while attempting to reach the desired test conditions.

The results discussed so far, both present ones and Mouslim's, demonstrate that the occurrence of DHT in R134a may depend on the position of the selected point in CO_2 with respect to the peak. However, these results do not exclude the possibility that differences in the onset of DHT may also be due, at least in part, to inadvertent differences in the loop components and settings during the tests. The most intriguing evidence that contradicts the previously discussed findings is in Mouslim's Figures E.3 and E.4 (also in Figure 5 in Mouslim & Tavoularis (2019)). These results, correspond to case 6 in Table 4.1, in which the CO_2 wall temperature profile has a distinct peak region under DHT, followed by an extensive NHT region. Mouslim scaled many points, upstream of, on and downstream of the peak and found that in all cases the R134a profile was under NHT. To shed more light into this issue, we also conducted tests for case 6. Figure 5.7 shows that R134a wall temperature profiles obtained by scaling conditions at three CO_2 points that spanned most of the test section were all under DHT, albeit with peaks diminishing as the scaled point was moved downstream.

This demonstrates that the occurrence or not of DHT in R134a does not exclusively depend on the location of selected point in CO_2. In summary, although we cannot evaluate unequivocally the success of the Ottawa method in scaling DHT from CO_2 to R134a, we may assert, based on the available results, that this method is likely to predict DHT in R134a, when the scaled point in CO_2 is in a DHT region, and less likely, as this point is moved farther downstream of the DHT region.

5.2.2 Pisa-method scaling

First, we examined whether the Pisa method consistently produced DHT wall temperature profiles in R134a when scaling DHT profiles in CO_2, irrespective of the shape of the profile and the accuracy in heat transfer prediction. All such tests, as shown in Figures 5.2, 5.3, 5.4, 5.6, and 5.7, confirmed the success of the Pisa method in this respect. Second, we examined whether the Pisa method consistently produced NHT profiles in R134a when scaling NHT profiles in CO_2 . Case 7P1, marked as 1 in Figure 5.8, contradicts such an assertion, as the CO_2 profile is clearly in NHT and the R134a profile is clearly in DHT. We performed additional tests at essentially fixed values of P, G, T_{in}, but gradually decreasing q, until we obtained NHT. This happened for case 7P2 in Table 4.1, which has a q that is 12% lower than the value in case 7P1. This observation demonstrates that the thresholds of conditions separating the prediction of NHT from that of DHT appear to span ranges rather than being sharp. As for the Ottawa method, we detected the presence of hysteresis in the value of the q threshold. It was found in the present work that the pressure difference between cases 7P1 and 7P2 was 1.4%, which is deemed to be sufficiently small not to have a significant effect on our conclusion. So again, the available results can be reconciled by assuming that the thresholds that separate NHT and DHT are not sharply defined but occupy relatively narrow ranges of conditions that depend on the experimental settings and methodology.

5.3 Nusselt number profiles

Selected axial profiles of the Nusselt number in CO_2, calculated from measurements by Kline (2017) (see also Kline & Tavoularis (2021)), and presently measured Nusselt

number profiles in R134a, scaled by the Ottawa and Pisa methods, are shown in Figures 5.10 to 5.16. As for the wall temperature profiles, each Nusselt number profile corresponds to a case number with conditions listed in Table 4.1. Visual inspection of corresponding CO_2 and R134a profiles in these figures shows that neither method provides a close match for any case. To quantify the match between reference and scaled profiles, we calculated the average ΔNu_{av} and the standard deviation $\sigma_{\Delta Nu}$ of differences ΔNu in Nusselt number values between corresponding tests in R134a and CO_2. Because the axial positions of thermocouples in the present R134a tests differed from those in the CO_2 reference tests, we used linear interpolation to calculate Nusselt number values for the present tests at the same 37 positions as the wall temperature measurements in the CO_2 tests. These results, normalised by the average Nu_{av} of all Nusselt number values in both corresponding CO_2 and R134a tests (i.e., 74 values for each case), are presented as percentages in Table 5.2.

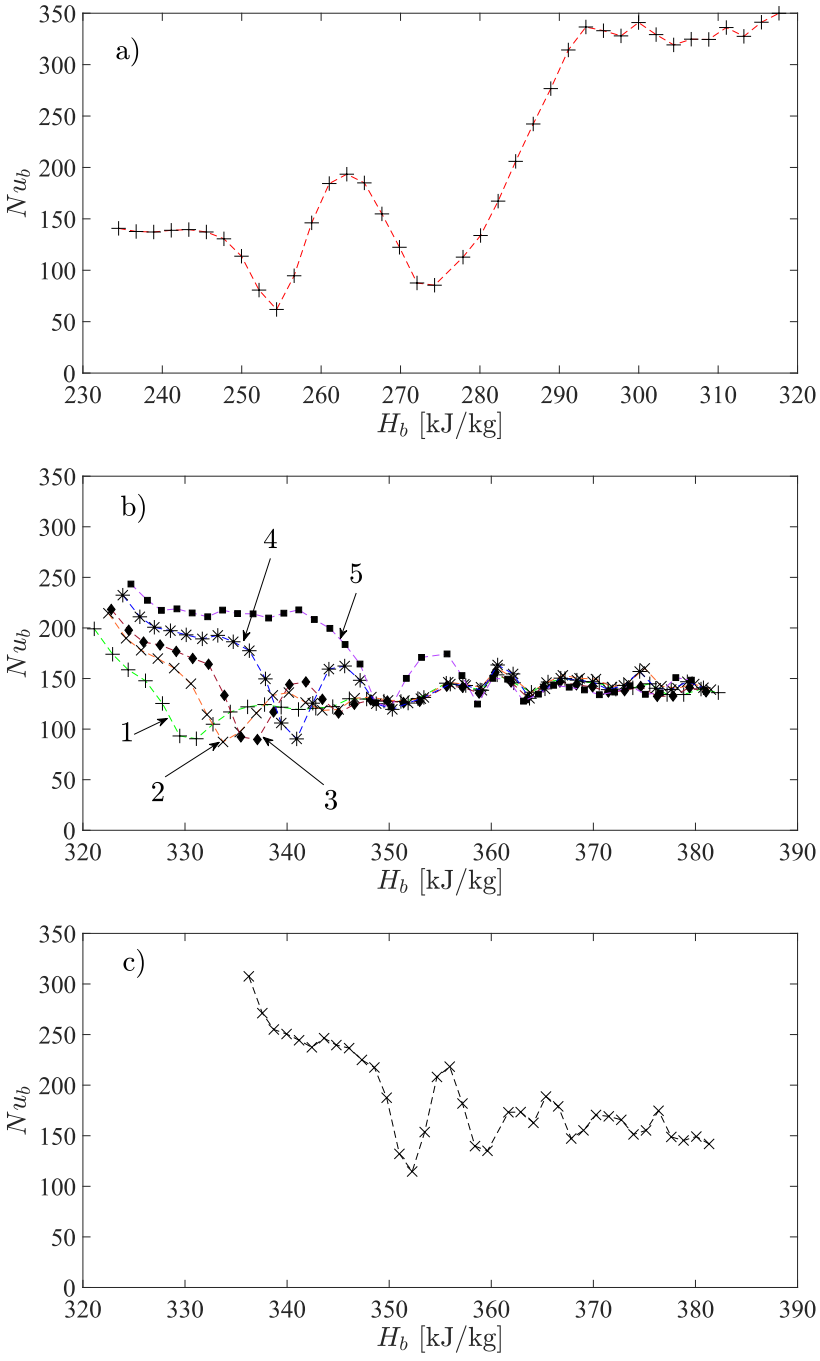

Figure 5.10: Nusselt number along the 8 mm tube containing a) CO_2; b) R134a scaled with the Ottawa method, and c) R134a scaled with the Pisa method. Test conditions are listed in Table 4.1, case 1.

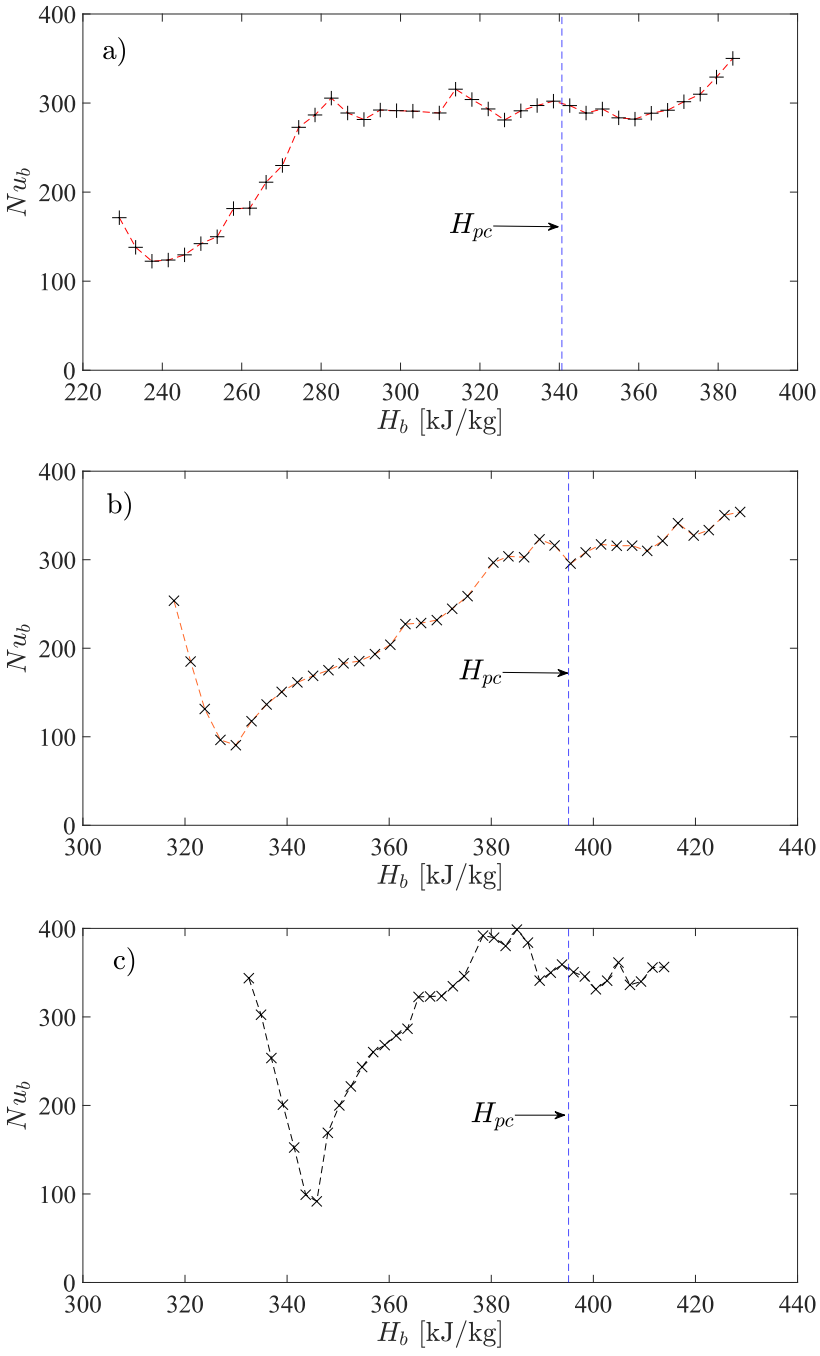

Figure 5.11: Nusselt number along the 8 mm tube containing a) CO_2; b) R134a scaled with the Ottawa method, and c) R134a scaled with the Pisa method. Test conditions are listed in Table 4.1, case 2.

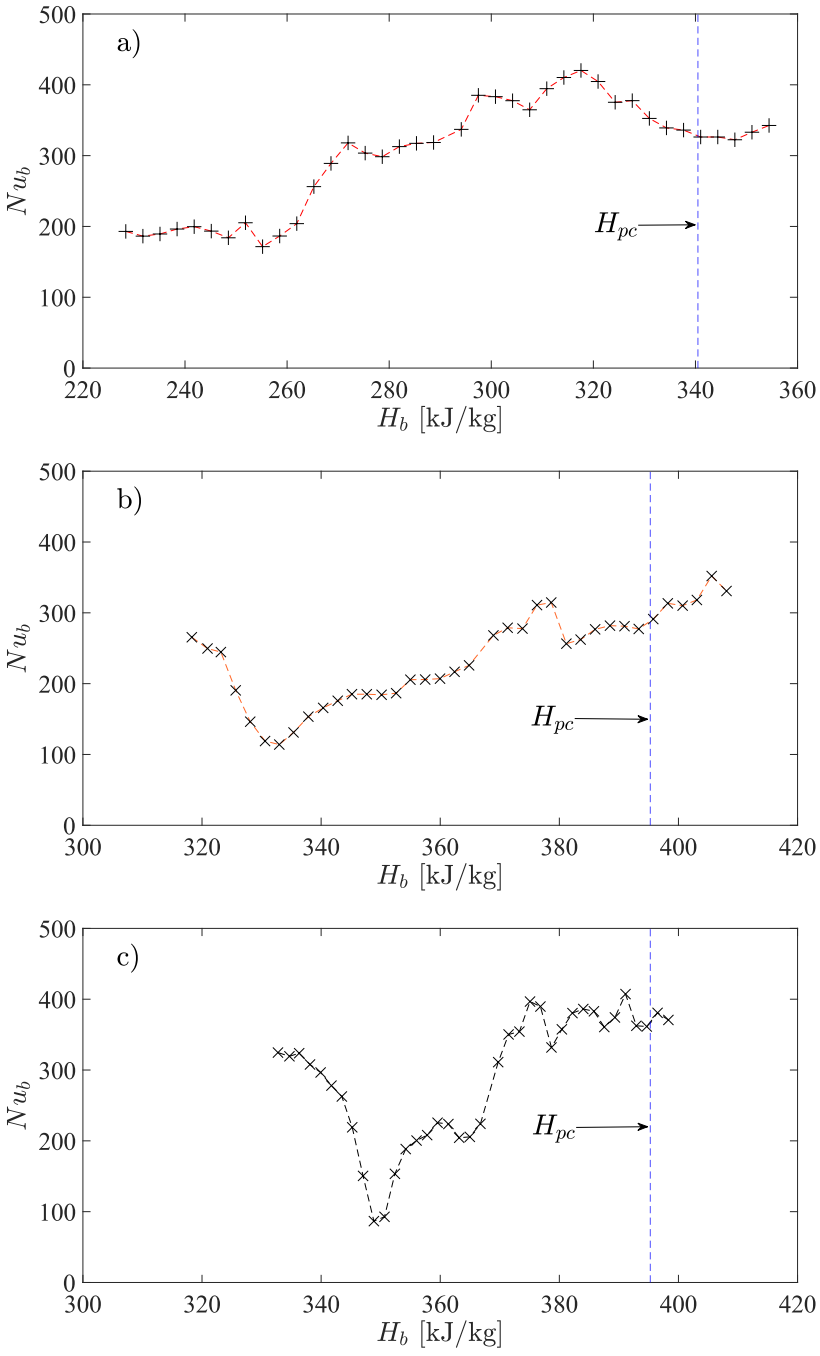

Figure 5.12: Nusselt number along the 8 mm tube containing a) CO_2; b) R134a scaled with the Ottawa method, and c) R134a scaled with the Pisa method. Test conditions are listed in Table 4.1, case 3.

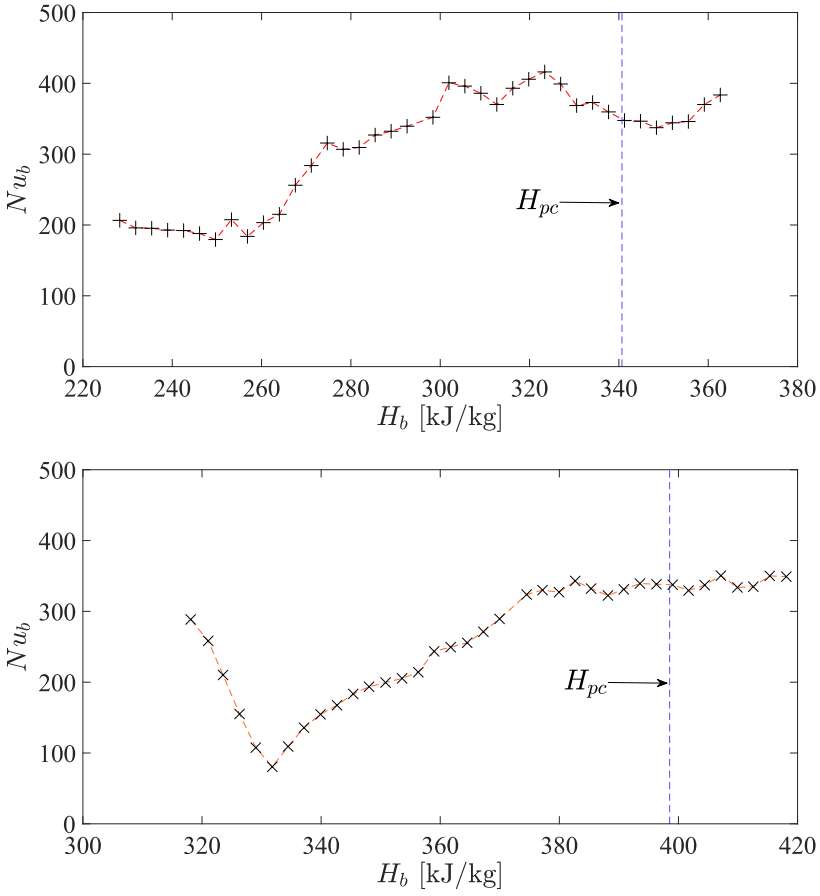

Figure 5.13: Nusselt number along the 8 mm tube containing a) CO_2 and b) R134a scaled with the Ottawa method. Test conditions are listed in Table 4.1, case 4.

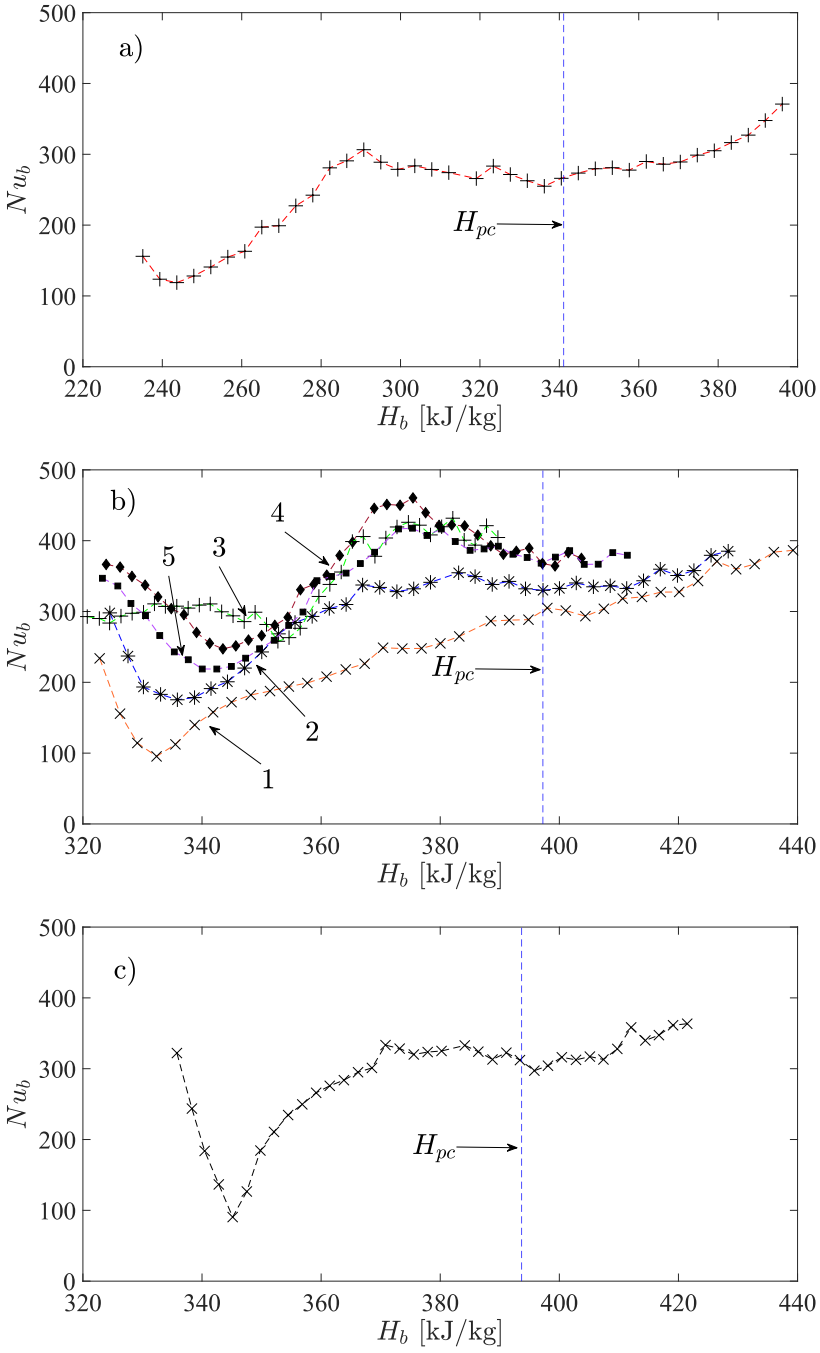

Figure 5.14: Nusselt number along the 8 mm tube containing a) CO_2; b) R134a scaled with the Ottawa method, and c) R134a scaled with the Pisa method. Test conditions are listed in Table 4.1, case 5.

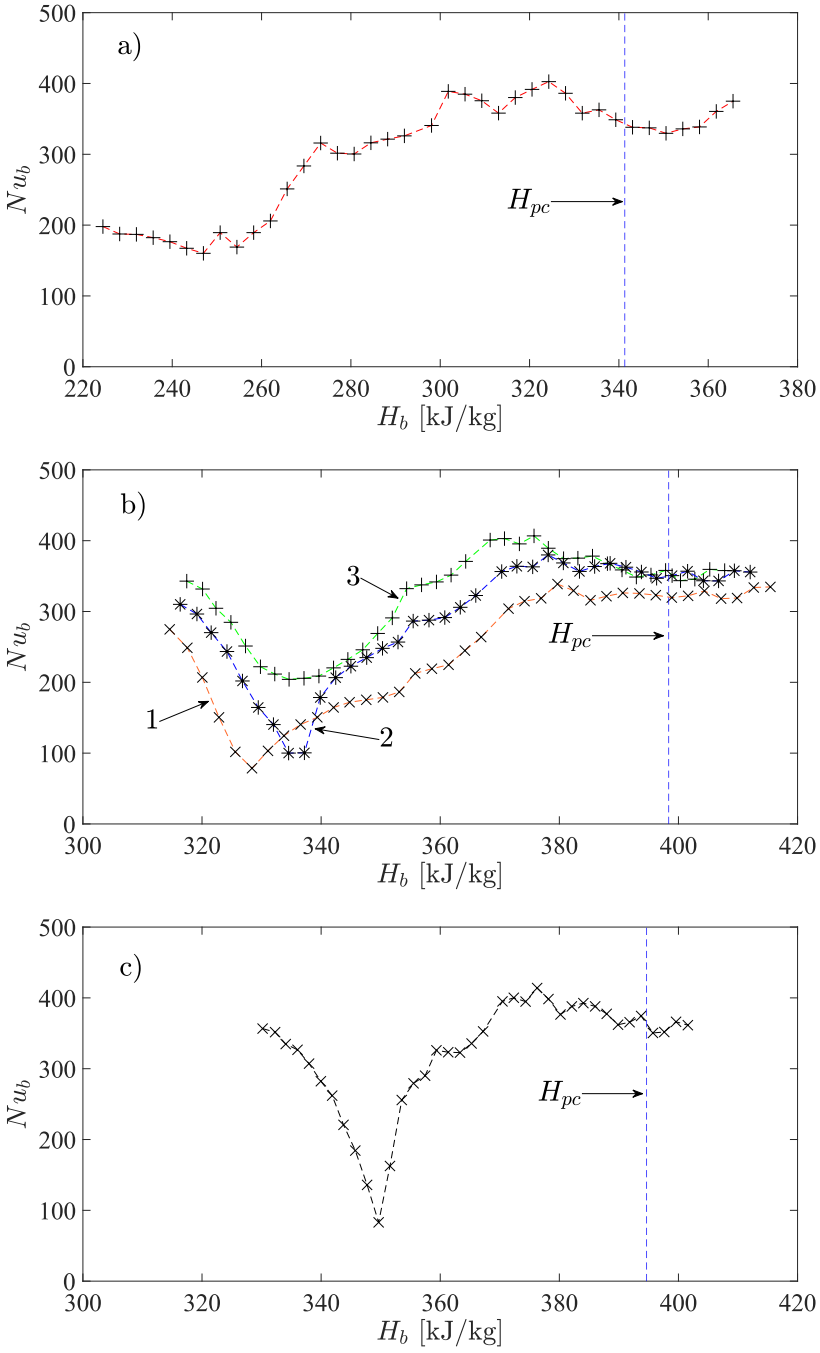

Figure 5.15: Nusselt number along the 8 mm tube containing a) CO_2; b) R134a scaled with the Ottawa method, and c) R134a scaled with the Pisa method. Test conditions are listed in Table 4.1, case 6.

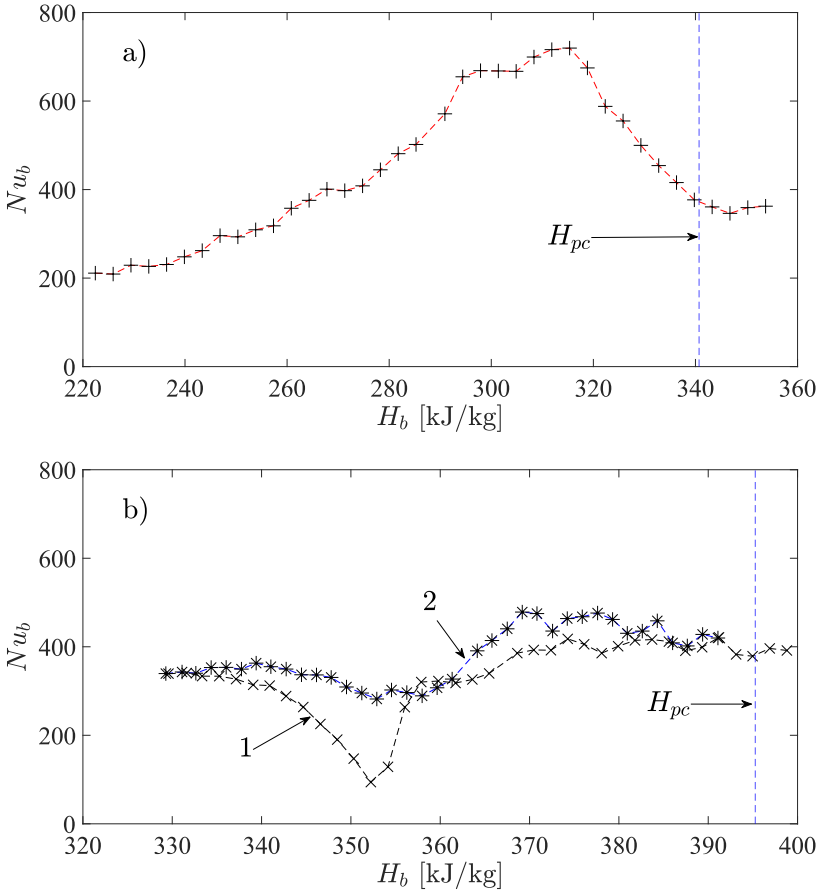

Figure 5.16: Nusselt number along the 8 mm tube containing a) CO_2 and b) R134a scaled with the Pisa method. Test conditions are listed in Table 4.1, case 7.

Case	Ottawa-method Scaling		Case	Pisa-method Scaling	
	$\Delta Nu_{av}/Nu_{av}$	$\sigma_{\Delta Nu}/Nu_{av}$		$\Delta Nu_{av}/Nu_{av}$	$\sigma_{\Delta Nu}/Nu_{av}$
1O1	-40.7%	68.8%			
1O2	-36.3%	66.1%			
1O3	-35.6%	68.1%	1P	-8.9%	65.7%
1O4	-28.5%	66.0%			
1O5	-17.5%	68.4%			
2O1	-3.1%	18.6%	2P	17.0%	24.4%
3O1	-24.2%	32.4%	3P	-2.4%	26.0%
4O1	-15.1%	21.0%	4P	N/A	
5O1	2.4%	17.8%			
5O2	18.6%	21.4%			
5O3	30.6%	36.7%	5P	13.5%	18.7%
5O4	34.8%	42.7%			
5O5	28.9%	36.0%			
6O1	-17.5%	23.8%			
6O2	-1.2%	14.0%	6P	9.1%	21.6%
6O3	8.4%	16.2%			
7O	N/A		7P1	-26.9%	45.8%
			7P2	-13.9%	35.7%

Table 5.2: Averages and standard deviations of differences in Nusselt number values between corresponding tests in CO_2 and R134a, normalised by the corresponding average Nusselt number in both CO_2 and R134a tests.

While assessing the differences between Nusselt numbers that were observed in the two fluids at nominally equivalent conditions, we must consider that such differences are the combined effects of several sources of discrepancy. These sources act simultaneously and their effects cannot be separated in an accurate manner, although some statistical bias and precision limits can possibly be devised in some cases. Uncertainty limits are added in the mean square, but each source may contribute positively or negatively to each individual value of the total difference and also each contribution may have systematic and total parts. We shall not attempt to separate the various effects, but merely identify their sources, as outlined in the following list.

- Inaccuracy of the scaling method: This is of course the main interest in this work. If other effects were absent or corrected for, this inaccuracy would have been quantifiable by the measurements.

- Measurement errors: Measurable or estimable errors were corrected for, but the results certainly contain both systematic and random errors, which ideally can be quantified statistically, but it is hard to do so. Examples include interference and electronic noise, instrument cross-talk, and calibration errors.

- Differences between actual and ideal scaled conditions.

- Effects of history of past measurements and hysteresis.

In the following discussion, we will present some general observations on the quantitative capabilities of the Ottawa and Pisa methods, albeit with the understanding that these observations are based on a relatively small number of tests, performed under relatively narrow ranges of conditions. These assertions may have been different in some ways, had they been based on studies with a much wider scope.

- For both the Ottawa and Pisa methods, both positive and negative average differences were observed, within the range from -40.7% to +18.6%, so we may not conclude that scaling by either method introduces a strong positive or negative bias.

- Overall, the Ottawa method tends to underestimate the average Nu in more cases and by larger percentages than the Pisa method.

- The Nu fluctuations along the test section tend to vary by around $20 - 30\%$ for both methods, except for case 1, in which they are at least twice as large. It is noted that case 1 has a significantly lower mass flux than the other cases and may be subject to larger uncertainties, including those of the NIST tables. Much of the discrepancy in case 1 is caused by the fact that the Nu level in the CO_2 tests was elevated in the downstream half of the test section, possibly indicating the occurrence of enhanced heat transfer, whereas in the R134a tests the Nu level did not change much along the test section. Perhaps some of the Nu difference is due to limitations of scaling for enhanced heat transfer, but much more information is needed before a conclusive statement can be made on this possibility.

- For the Ottawa method, it was observed that, in general, the average difference between the Nusselt numbers in the two fluids tended to increase as the test point was picked farther downstream from the peak.

- The results of the Ottawa method for case 6 (Figure 5.15) show that point 2 provided the lowest among all differences in both averages and standard deviations of Nu. Without additional tests, it is not possible to assess whether this is coincidental or has something to do with the particular conditions for this case. A possible topic for future tests would be to investigate whether there is a pattern from which one may predict the location of optimum scaling.

Chapter 6

Conclusions and recommendations for future research

6.1 Conclusions

Experimental evaluations of two fluid-to-fluid scaling methods for deteriorated heat transfer in upward vertical flows in tubes at supercritical pressures were performed at the University of Ottawa Supercritical Heat Transfer Loop (SCUOL), using Refrigerant R134a as a medium at conditions that were determined by scaling those in previous carbon dioxide tests in the same loop. Two scaling methods were used to obtain test conditions: the Ottawa method and the Pisa method. The following main conclusions were drawn based on the results from these tests.

- Both the Ottawa and the Pisa scaling methods were partially successful in scaling the occurrence or absence of DHT, but only when allowing for the thresholds of DHT onset conditions to span some ranges rather than being sharply defined.

- Neither method was accurate in predicting the exact location of DHT in the tube or the value of the local heat transfer coefficient.

- Some hysteresis was present in the onset of DHT.

The present assessment of the Ottawa method is consistent largely with the assessment by Mouslim (2019), but we have revisited, clarified and modified some conclusions reached by that author, as well as performing new tests that extended the previous range of conditions. The present experimental assessment of the Pisa method and the observed hysteresis in the onset of DHT are entirely novel results.

6.2 Recommendations for future work

The following is a list of recommendations for future work.

- Perform additional tests for wider ranges of mass flux and heat flux. Also perform tests at different pressures.

- Further investigate the effect of hysteresis upon the onset of DHT. Systematic measurements should be taken near the onset of DHT at different values of mass flux and heat flux. By increasing and reducing the heat flux at these conditions, DHT will be observed to occur and disappear at different combinations of values of mass flux and heat flux, depending on its direction of change. With sufficient number of results, one may generate a two-dimensional map, identifying DHT regions of conditions, with gray shading of regions affected by hysteresis.

- Further test the Pisa scaling law using an iterative approach on the heat flux as suggested by Pucciarelli & Ambrosini (2020). These authors point out that their method contains approximations and the scaling relationship for heat flux may not model exactly the underlying physical mechanism. This was indeed seen in the present work in case 7 in Table 4.1. Investigating this issue over a broad range of conditions, particularly mass flux, would help resolve it.

- Test the scaling methods using different fluids, such as R23 or NH_3, which have thermophysical behaviours that are not very different from that of water.

References

Ambrosini, W. 2011 Discussion of Similarity Principles for Fluid-to-Fluid Scaling of Heat Transfer Behaviour at Supercritical Pressures. *Nucl. Eng. Des.* **241** (12), 5149 – 5173.

American Society for Testing and Materials 2011 Standard specification and temperature-electromotive force (emf) for standardized thermocouples. https://cdn.standards.iteh.ai/samples/77682/a7613eaafb804e519f4d7926339a2423/ASTM-E230-E230M-11.pdf, 2024-09-06.

Azih, C. & Yaras, M. I. 2017 Similarity Criteria for Modeling Mixed-Convection Heat Transfer in Ducted Flows of Supercritical Fluids. *J. Heat Transfer* **139** (12), 122501.

Cheng, X., Liu, X.J. & Gu, H.Y. 2011 Fluid-to-Fluid Scaling of Heat Transfer in Circular Tubes Cooled with Supercritical Fluids. *Nucl. Eng. Des.* **241** (2), 498 – 508.

ECC-Smart & ENEN 2020 ECC-SMART project. https://ecc-smart.eu/about/, accessed: 2024-10-17.

Government of Canada 2022 Reporting a release of a halocarbon. https://publications.gc.ca/collections/collection_2022/eccc/En14-488-7-2022-eng.pdf, accessed: 2024-07-29.

Jackson, J. D. & Hall, W. B. 1978 *Influence of Buoyancy on Heat Transfer to Fluids Flowing in Vertical Tubes Under Turbulent Conditions*, *Turbulent Forced Convection in Channels and Bundles*, vol. 2. New York, NY: McGraw-Hill International Book Company.

Jevremovic, T. & Rehman, H. 2021 New crp: Advancing thermal-hydraulic models and predictive tools for design and operation of scwr prototypes (i31034). https://www.iaea.org/newscenter/news/new-crp-advancing-thermal-hydraulic-models-and-predictive-tools-for-design-and-operation-of-scwr-prototypes-i31034, accessed: 2024-10-16.

Jiang, K. 2015 An Experimental Facility for Studying Heat Transfer in Supercritical Fluids. Master's thesis, University of Ottawa, Ottawa, Canada.

Kassem, S., Puciarelli, A. & Ambrosini, W. 2021 Extending a fluid-to-fluid similarity rationale for heat transfer at supercritical pressure to R134a. In *Proceedings of the 2021 28th International Converence on Nuclear Engineering (ICONE28)*. Amer Soc Mech Engineers; Amer Soc Mech Engineers, Nucl Engn Div.

Kline, N. 2017 An Experimental Study of Heat Transfer Deterioration at Supercritical Pressures. Master's thesis, University of Ottawa, Ottawa, Canada.

Kline, N., Feuerstein, F. & Tavoularis, S. 2018 Onset of Heat Transfer Deterioration in Vertical Pipe Flows of CO_2 at Supercritical Pressures. *Int. J. of Heat Mass Transfer* **118**, 1056 – 1068.

Kline, N. & Tavoularis, S. 2017 A Heat Transfer Database for Supercritical Carbon Dioxide Flowing in Three Directly Heated Tubes With Internal Diameters Equal to 4.6, 8.0, and 22.0 mm Under Closely Incremented and Widely Ranging Operating Conditions.

Kline, N. & Tavoularis, S. 2021 On the Use of a Buoyancy Parameter for Distinguishing Deteriorated from Normal Heat Transfer in Upward Flows at Supercritical Pressures. *J. Fluids Eng.* **143**.

Lemmon, E. W., McLinden, M. O. & Friend, D. G. 2002 *Thermophysical Properties of Fluid Systems*. National Institute of Standards and Technology (NIST), NIST Standard Reference Database Number 69, NIST Reference Fluid Thermodynamics Properties Database (REFPROP): Version 7.0, 2002.

Mouslim, A. 2019 Tests of Fluid-to-Fluid Scaling Laws for Supercritical Heat Transfer. Master's thesis, University of Ottawa, Ottawa, Canada, publication Title: M.A.Sc., Thesis.

Mouslim, A. & Tavoularis, S. 2019 Direct tests of fluid-to-fluid scaling expressions for supercritical heat transfer in tubes. *Int. J. Heat Mass Transfer* **147** (1).

Oettig, J., Licht, L., Ferrand, T., Westermeier, M., Schifflechner, C., Pioro, I. & Spliethoff, H. 2024 Experimental investigation of phenomena in heat transfer to water at near critical pressures. In *Proceedings of the 14th International Topical Meeting on Nuclear Reactor Thermal-Hydraulics, Operation and Safety (NUTHOS-14)*.

Pioro, I. L. & Duffey, R. B. 2007 *Heat Transfer and Hydraulic Resistance at Supercritical Pressures in Power Engineering Applications*. New York, NY, USA: ASME Press.

Pioro, I. L., Mokry, S. & Draper, S. 2011 Specifics of Thermophysical Properties and Forced-Convective Heat Transfer at Critical and Supercritical Pressures. *Rev. Chem. Eng.* **27** (3-4), 191–214.

Pucciarelli, A. & Ambrosini, W. 2016 Fluid-to-Fluid Scaling of Heat Transfer Phenomena with Supercritical Pressure Fluids: Results from RANS Analyses. *Ann. Nucl. Energy* **92**, 21–35.

Pucciarelli, A. & Ambrosini, W. 2020 A Successful General Fluid-to-Fluid Similarity Theory for Heat Transfer at Supercritical Pressure. *Int. J. Heat Mass Transfer* **159**.

Son, S. & Lee, J. I. 2024 Feasibility and performance limitations of Supercritical carbon dioxide direct-cycle micro modular reactors in primary frequency control scenarios. *Nucl. Eng. Technol.* **56** (4), 1254–1266.

Uchimura, K. & Yamaji, A. 2020 Preliminary Core Design Study of Small Supercritical Fast Reactor with Single-Pass Cooling. *J. Nucl. Eng.* **1** (1), 46–53.

Watts, M. J. & Chou, C. T. 1982 Mixed Convection Heat Transfer to Supercritical Pressure Water. In *Proceedings of the Seventh International Heat Transfer Conference (IHTC)*, , vol. 3, pp. 495–500. Munich, Germany.

Zahlan, H., Groeneveld, D.C. & Tavoularis, S. 2014 Fluid-to-Fluid Scaling for Convective Heat Transfer in Tubes at Supercritical and High Pressures. *Int. J. Heat Mass Transfer* **73** (1), 274–283.

Appendix A

Selected reference figures

This appendix contains figures from Mouslim (2019) that overlap with cases in the present work.

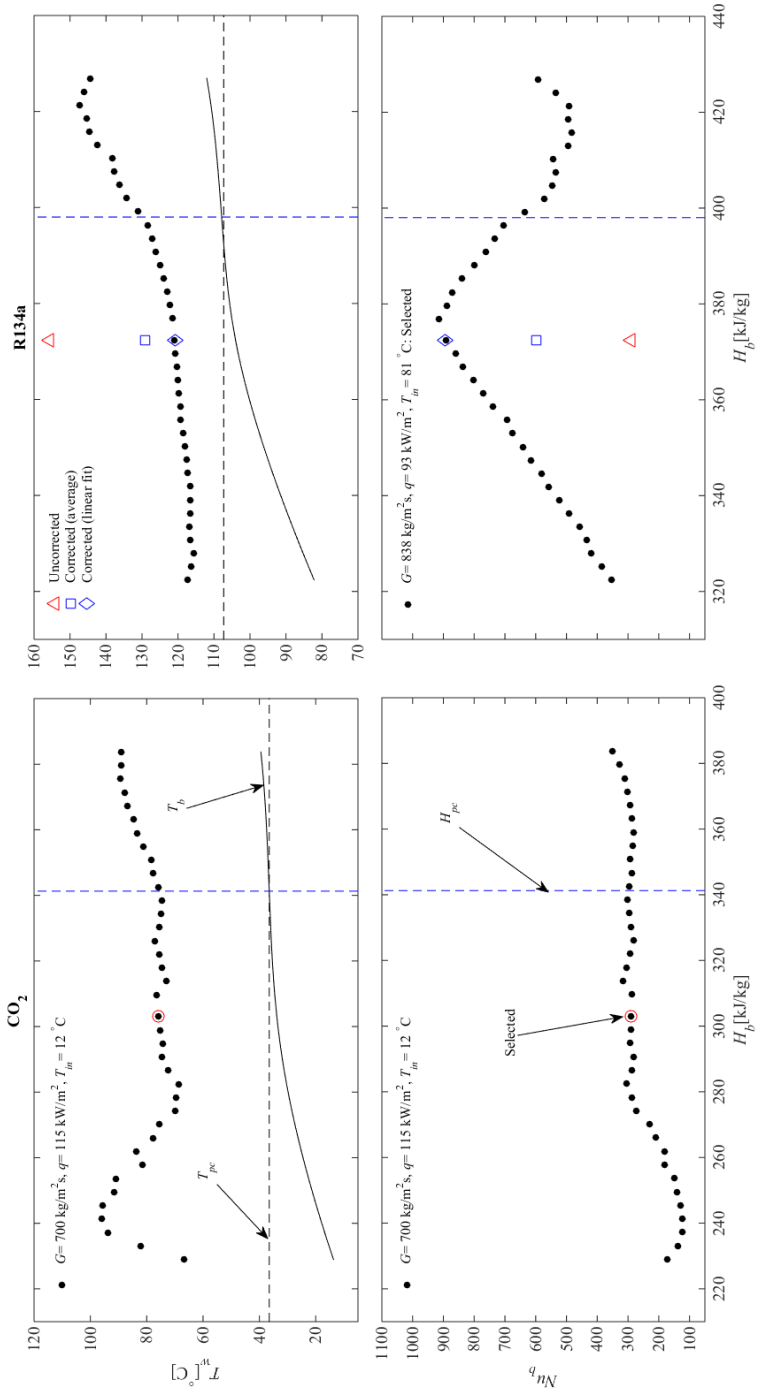

Figure A.1: Measurements of wall temperature (top) and bulk Nusselt number (bottom) *vs.* bulk enthalpy profiles in the fluids CO_2 and R134a at equivalent conditions for NHT; CO_2 test condition: $G = 700$ kg/m^{2}s , $q = 115$ kW/m^2, $T_{in} = 12$°C (Figure E.1 in Mouslim (2019); also present case 2 in table 4.1).

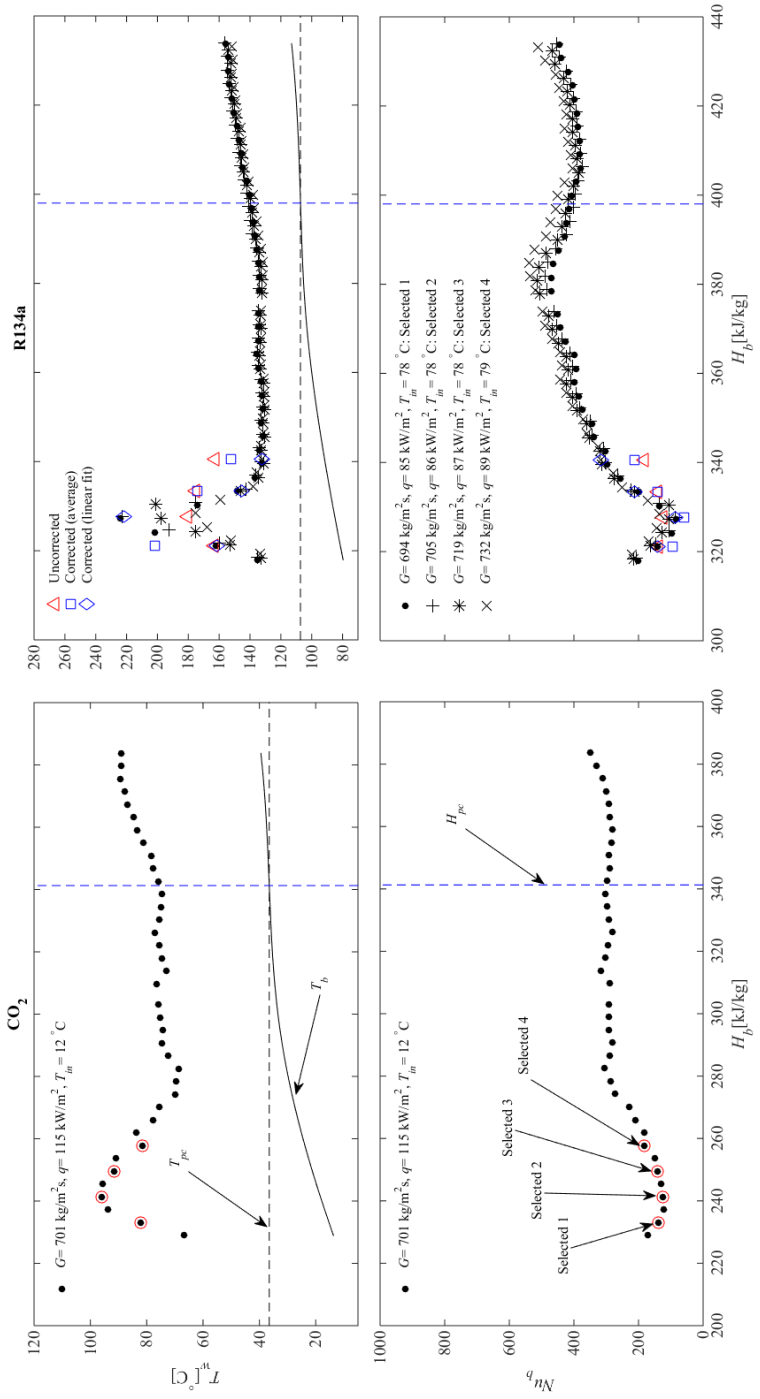

Figure A.2: Measurements of wall temperature (top) and bulk Nusselt number (bottom) *vs.* bulk enthalpy profiles in the fluids CO_2 and R134a at equivalent conditions for NHT; CO_2 test condition: $G = 701$ kg/m^{2}s , $q = 115$ kW/m^2, $T_{in} = 12$°C (Figure E.6 in Mouslim (2019); also present case 2 in table 4.1).

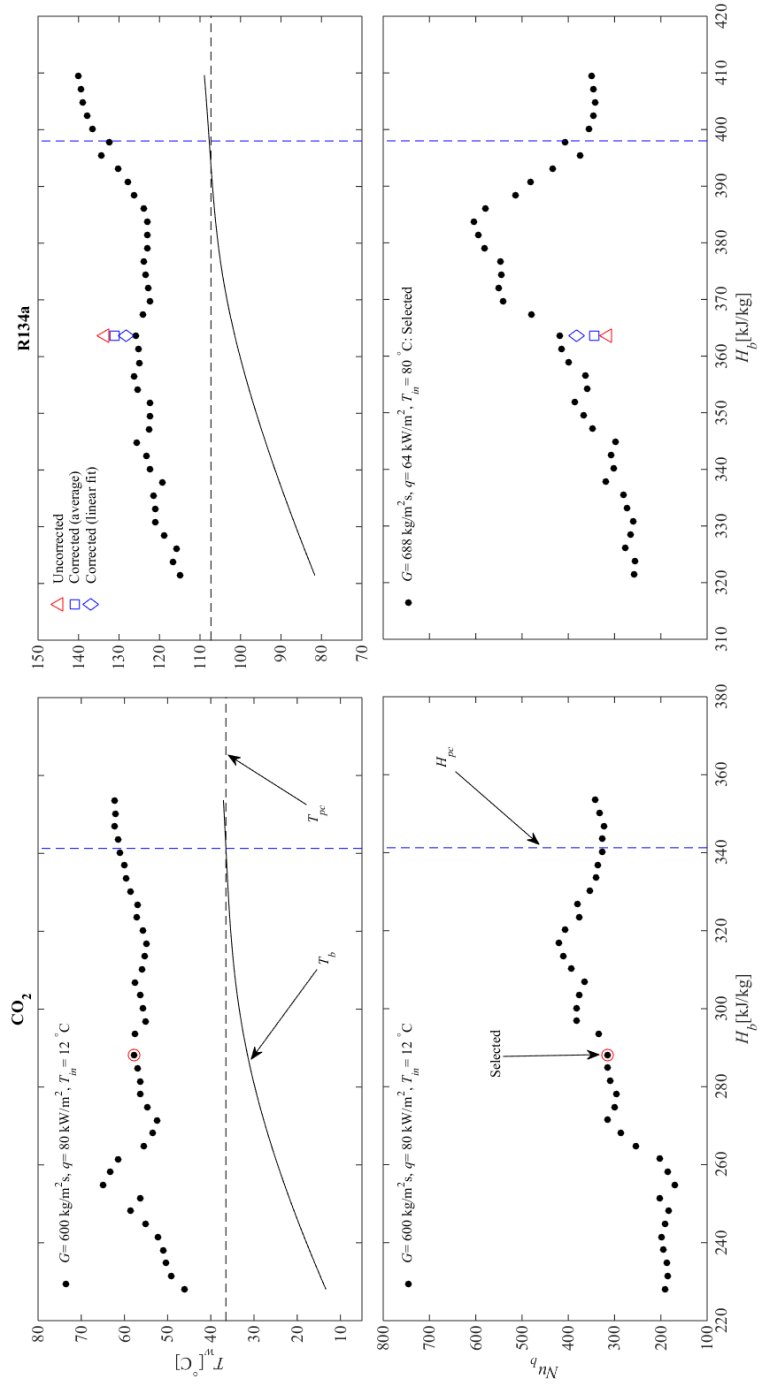

Figure A.3: Measurements of wall temperature (top) and bulk Nusselt number (bottom) *vs.* bulk enthalpy profiles in the fluids CO_2 and R134a at equivalent conditions for NHT; CO_2 test condition: $G = 600$ kg/m^{2}s , $q = 80$ kW/m^2, $T_{in} = 12$°C (Figure D.21 in Mouslim (2019); also present case 3 in table 4.1).

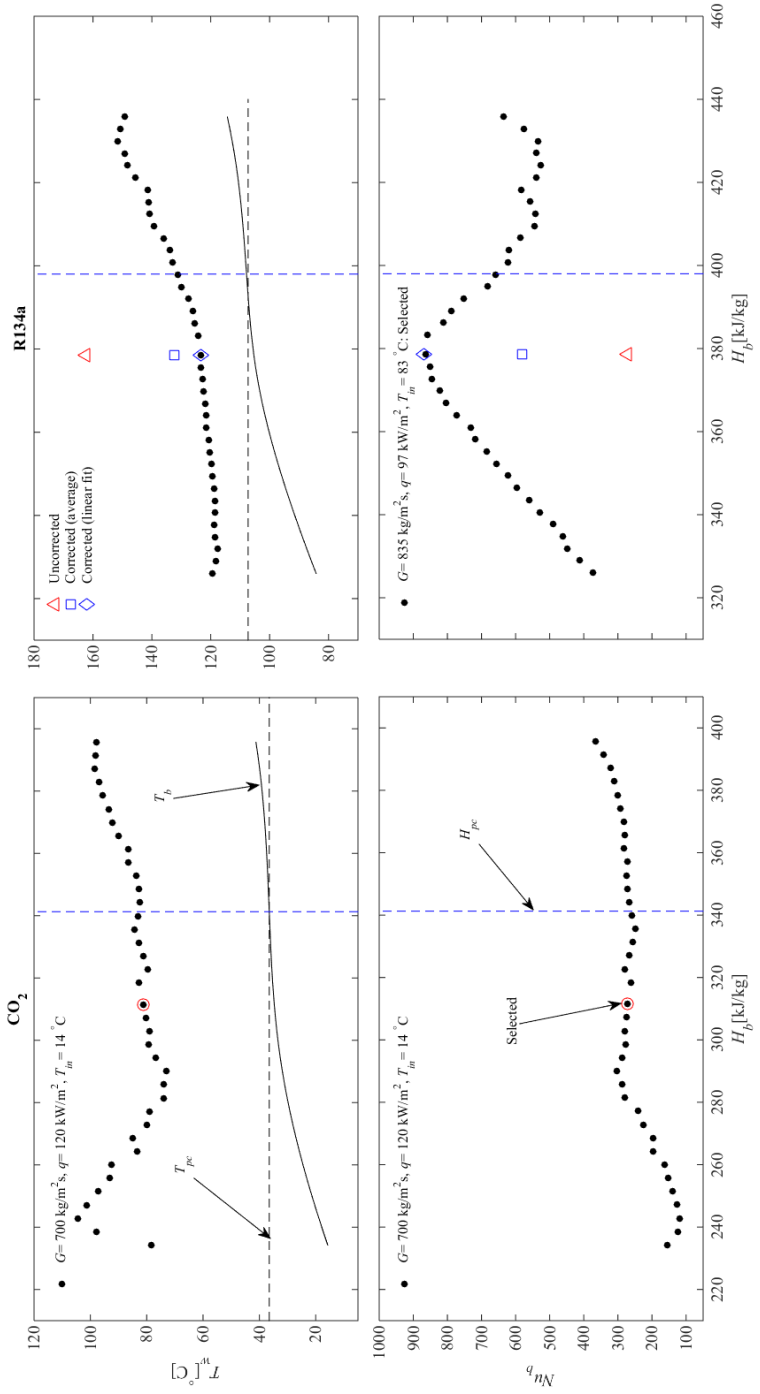

Figure A.4: Measurements of wall temperature (top) and bulk Nusselt number (bottom) *vs.* bulk enthalpy profiles in the fluids CO_2 and R134a at equivalent conditions for NHT; CO_2 test condition: $G = 700$ kg/m^{2}s , $q = 120$ kW/m^2, $T_{in} = 14$°C (Figure E.2 in Mouslim (2019); also present case 5 in table 4.1).

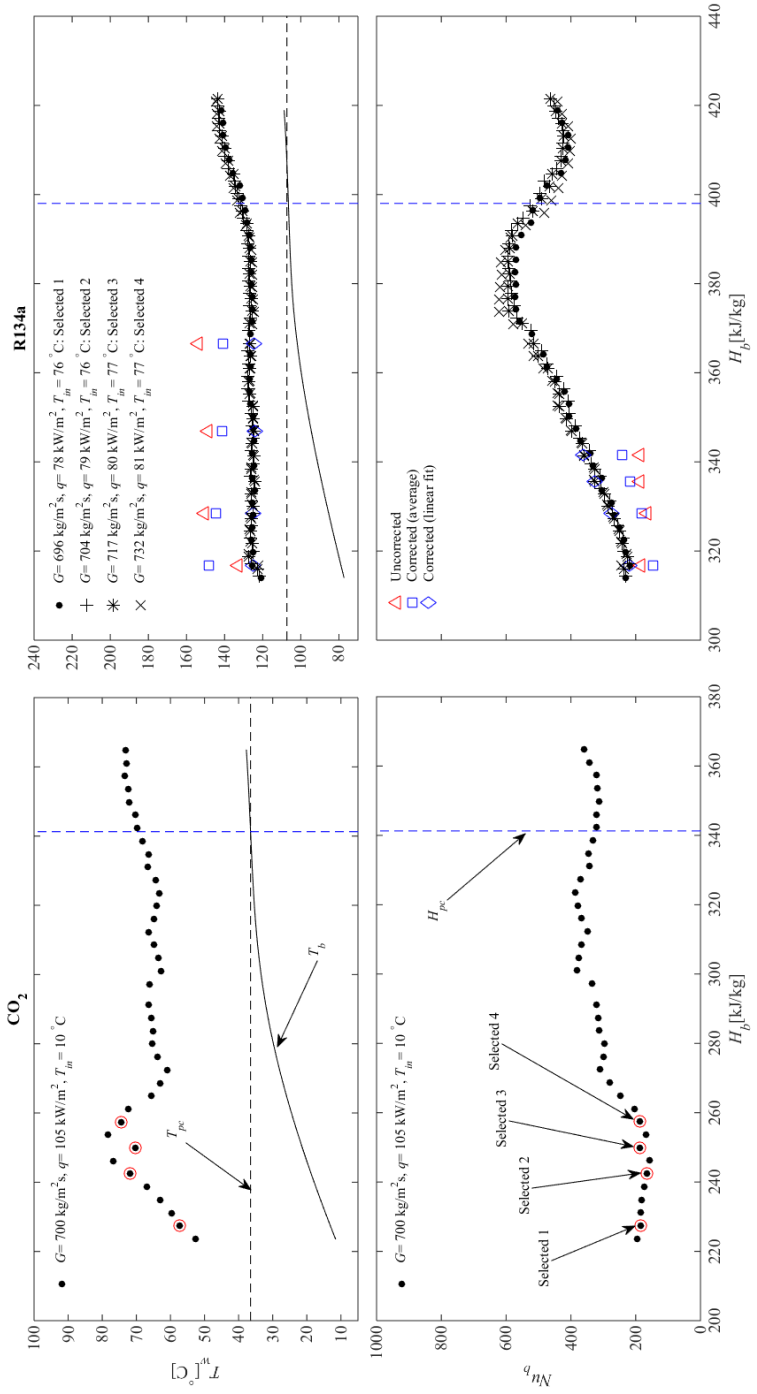

Figure A.5: Measurements of wall temperature (top) and bulk Nusselt number (bottom) *vs.* bulk enthalpy profiles in the fluids CO_2 and R134a at equivalent conditions for NHT; CO_2 test condition: $G = 700$ kg/m^{2}s , $q = 105$ kW/m^2, $T_{in} = 10$°C (Figure E.3 in Mouslim (2019); also present case 6 in table 4.1).

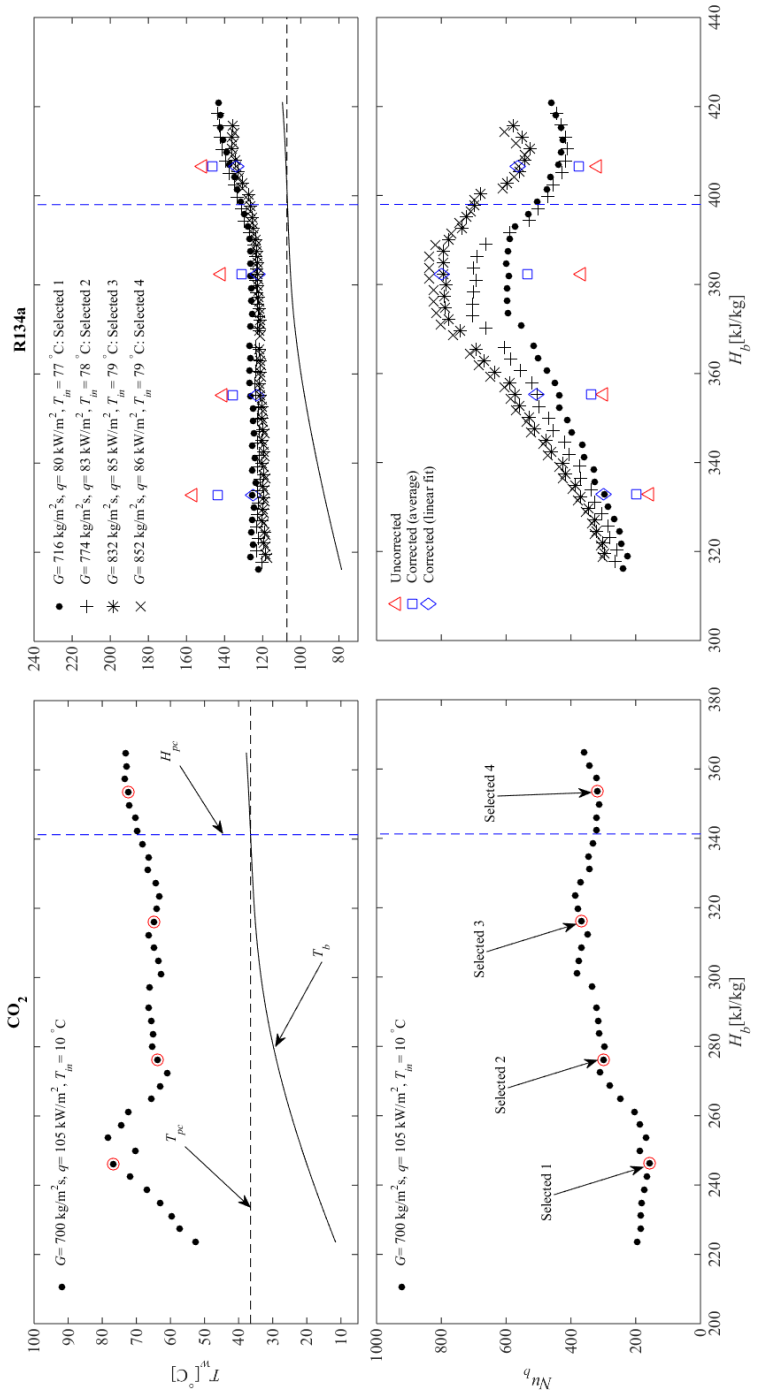

Figure A.6: Measurements of wall temperature (top) and bulk Nusselt number (bottom) *vs.* bulk enthalpy profiles in the fluids CO_2 and R134a at equivalent conditions for NHT; CO_2 test condition: $G = 700$ kg/m^{2}s , $q = 105$ kW/m^2, $T_{in} = 10$°C (Figure E.4 in Mouslim (2019); also present case 6 in table 4.1).